Disturbance Observer-Based Robust Current Control Scheme for Three-Phase Grid-Tied Inverters With *LCL* Filter Considering Unbalanced Grid Voltages

Amulya Viswambharan, Rachid Errouissi, *Senior Member, IEEE*, Mahdi Debouza, *Student Member, IEEE*, Hussain Shareef, *Member, IEEE*, and Addy Wahyudie, *Member, IEEE*

***Abstract*—This article presents a comprehensive study on the design, robust stability analysis, performance evaluation, and real-time implementation of a disturbance observer-based controller for grid-connected voltage-source inverters (VSIs) with *LCL* filter. The proposed composite controller integrates a state-feedback controller with a disturbance observer to enhance the tracking performances of grid-tied inverter with *LCL* filter. The grid-tied VSI is modeled in the stationary reference frame ($\alpha\beta$) to accommodate both balanced and unbalanced grid voltages. The main objective of the proposed approach is to achieve asymptotic tracking of sinusoidal references in the presence of unknown disturbances and parametric uncertainties. More precisely, not only does the controller ensure accurate tracking performances, but also it can maintain closed-loop stability and good transient performances in the presence of model uncertainties. Moreover, the integration of control saturation in the observer design makes it possible to mitigate the effect of control saturation during transients without the need for designing an antiwindup scheme. The effectiveness of the composite controller is validated through numerical simulation and experimental implementation. The results demonstrate high-performance characteristics in terms of tracking accuracy and robustness to parameter variations in the presence of balanced grid voltages, unbalanced grid voltages, and control saturation.**

***Index Terms*—Disturbance observer, feedback-linearization, grid-tied inverter, *LCL* filter, renewable energy, robust controller.**

I. Introduction

IN POWER electronic interfaced renewable energy conversion systems, voltage-source inverter (VSI) facilitates the connection between power sources and the utility grid. As the central component of the system, VSI is charged with the task of stable and efficient injection of high-quality current into the power grid. Such a task can be achieved by using an LCL filter as shown in Fig. 1 because of its smaller size and superior harmonic attenuation in comparison with other filter types [1]. However, the inherent resonance frequency of the LCL filter makes it challenging to control the current injection into the grid.

Received 27 March 2024; revised 12 June 2024 and 22 August 2024; accepted 8 October 2024. Date of publication 11 October 2024; date of current version 18 December 2024. Recommended for publication by Associate Editor S. Ali Khajehoddin. *(Corresponding author: Rachid Errouissi.)*

The authors are with the Electrical Engineering, Department of College of Engineering, United Arab Emirates University, Al Ain 15551, UAE (e-mail: 202090007@uaeu.ac.ae; rachid.errouissi@uaeu.ac.ae; 202190014@uaeu.ac.ae; shareef@uaeu.ac.ae; addy.w@uaeu.ac.ae).

Color versions of one or more figures in this article are available at https://doi.org/10.1109/TPEL.2024.3478336.

Digital Object Identifier 10.1109/TPEL.2024.3478336

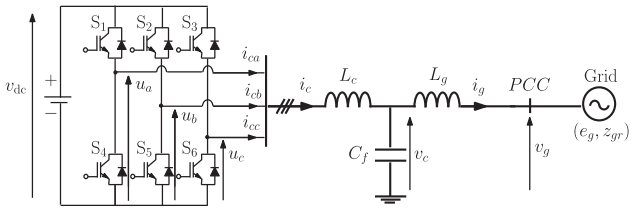

Fig. 1. Typical topology of grid-tied VSI with *LCL* filter in renewable energy systems (RESs). Here, PCC stands for point of common coupling. e_g and Z_{gr} are the actual grid voltage and grid impedance, respectively.

Various techniques have been proposed for addressing resonance issue in LCL filters. Passive active method, consisting of adding resistors in series or parallel with filter elements, is among the early techniques for mitigating the resonance problem in LCL filters. This technique is able to provide reliable solutions, but at the expense of increased power losses [2]. The increase of power loss with passive damping methods has motivated employing alternative damping techniques to avoid adding external resistors to LCL filters. Among these techniques are active damping methods which manipulate the control system to achieve resonance attenuation without incurring additional power losses [3], [4], [5]. Within this context, a multitude of controllers, complemented by active damping methods, are presented in the literature such as proportional-integral (PI) control [6], proportional-resonant (PR) control [7], [8], [9], repetitive control [10], sliding mode control (SMC) [11], [12], model predictive control [13], [14]. In addition, addressing physical system uncertainties and external disturbances is essential to ensure stable, robust, and accurate control of grid-connected VSI. This is because any variations in system parameters or alterations in grid impedance can lead to changes in the resonance frequency, degrade the grid-injected current, and even destroy the stability of the closed-loop system. This work is mainly focused on designing a robust current controller for grid-tied inverter with LCL filter, where both stability and performance specifications can be retained under a wide range of parameters variations.

The literature reports several research works that employ robust control approaches to cancel the effect of model uncertainties, parameters variations, and unknown external disturbances in grid-tied inverter with LCL filter. Robust predictive control techniques described in [15] and [16] demonstrated how

well such techniques work to handle uncertainties in system's parameters through the integration of adaptive control laws and the deadbeat algorithm. The utilization of a multiloop framework in implementing Lyapunov-function-based control, as discussed in [17], contributes to enhanced global stability for a narrow range of LCL parameter variations. Within the realm of nonlinear controllers, SMC has gained a significant attention for its commendable attributes, including rapid dynamic response and resilience against parameter variations. In [18], a multiple sliding surface approach was used to ensure good performances in the presence of unbalanced and distorted grid conditions, which was achieved at the expense of increasing hardware complexity and creating chattering problem. In [19], a pulse width modulation (PWM)-SMC controller was applied to LCL filter aimed to achieve robustness against output filter parameter drift and chattering problem. An alternate approach to provide optimal robust stability against power grid impedance changes was presented in [20], where a dedicated H_∞ controller was developed for LCL filtered grid-connected VSI. In [21], a multivariable H_∞ control framework was employed to design a robust and optimal controller for power converters. This framework seeks to regulate the inverter output current rather than the grid current, which could lead to high-frequency oscillations if the inverter switching frequency closely aligns with the resonant frequency. In [22], [23], and [24], linear matrix inequalities (LMIs) are employed to synthesize a state feedback controller incorporating H_∞ performance aiming to ensure robust damping in the presence of parametric uncertainties. However, the introduction of supplementary LMI constrains tends to amplify the conservatism in the design procedure. This often results in a high gain set of control parameters, which can create difficulties in real-time implementation.

The aforementioned controllers have been mostly designed to maintain asymptotic stability of the closed-loop system in the presence of model uncertainties, without giving attention to the effect of parameters variations on the transient response specifications. Literature review reveals that the use of disturbance/uncertainty estimation and attenuation (DUEA) approach can ensure robust and accurate control, while almost meeting the performance specifications on the transient response in the presence of modeling errors. This approach incorporates a two-degree-of-freedom control framework, providing the advantages of decoupled tracking and disturbance rejection [25]. Such an approach has been applied in [26] through the use of an extended state observer with the aim of robustly controlling grid-tied inverter under unbalanced grid voltages. The same concept has been employed in [27] to address resonance phenomena in LCL filter through the estimation of output and lumped disturbances. In [28], direct discrete-time pole placement was used to design a composite controller consisting of state/disturbance observer and feedback controller for grid-tied inverter with LCL filter. Although demonstrating good performances over a broad spectrum of filter parameter changes, the unexpected grid environment complicates the control operation [27]. In [29], a robust dichotomy technique based on extended Kalman filtering (EKF) has been employed to enhance the overall robustness of the system. However, setting the gains of an EKF can be a challenging task. Another approach of implementing DUEA technique is known as disturbance observer-based control (DOBC) which is becoming more popular in power electronic converter applications because of its improved disturbance rejection and reduced dependence on system models [28], [30], [31], [32], [33]. DOBC approach can also provide tighter guarantees on transient response specifications through the use of high observer gain because of its rapid rejection of the effect of unknown disturbances and modeling uncertainties [34]. Another feature of the DOBC is its ability to mitigate the effect of control saturation during transients [35].

This article proposes the use of DOBC approach to design a current controller for grid-tied VSI with *LCL* filter with a view to ensure good dynamics and accuracy under parameter variations and control saturation. The proposed current controller is developed in the $\alpha\beta$ stationary reference to cope with both balanced and unbalanced grid voltages. Compared with dq reference frame, the use of $\alpha\beta$ reference frame allows designing a less complex controller, capable of handling both balanced and unbalanced grid voltages without the need for additional control components. This partly explains why $\alpha\beta$ reference frame is adopted in this research work to design a composite current controller for the *LCL* filter. However, this mandates developing a controller that is capable of achieving the task of asymptotic tracking of sinusoidal references. Such a task can easily be achieved by combining a PR controller with either full-state feedback control or only capacitor current feedback [9]. The combined use of PR controller and feedback control has proved to be effective in achieving asymptotic regulation even in the presence of model uncertainty. The problem, however, is that model uncertainty, unknown disturbance, and control saturation during transients [36] can create difficulties for such a composite controller to maintain a good transient response. This difficulties can be reduced by using DOBC approach due to its ability to meet the transient response specifications even in the presence of model uncertainties, provided that the disturbance observer is fast enough [34]. This salient feature of DOBC is exploited in this work to realize high performance current controller for grid-tied VSI with *LCL* filter.

The main contributions of this article can be summarized as follows.

1) Design and experimental validation of a composite controller, consisting of a linear state-feedback control law and a disturbance observer, to maintain stable, accurate, and robust control of LCL filtered grid-tied VSI in the presence of model uncertainties, unbalanced grid voltages, and control saturation.
2) Employment of feedback linearization technique to derive the linear state-feedback control law, which has the advantage of providing a systematic way to select all control gains based on desired time-domain transient specifications.
3) Use of high-gain observer approach to design the disturbance observer, which requires only one design parameter, denoted here by ε, thus making the tuning process easier.
4) Analyze the stability of the nominal closed-loop system considering control saturation during transients.

5) Study the stability and robustness of the proposed controller through numerical investigation of the sensitivity of the closed-loop system to a wide range of parameters variations.
6) Compare the performances of the proposed composite controller with those of PR controller combined capacitor current feedback using numerical simulations.

The rest of this article is organized as follows. Section II introduces the state model of the LCL filtered grid-tied VSI in the $\alpha\beta$ reference frame, and presents the design procedure of the proposed composite controller. In Section III, the stability of the nominal closed-loop system is conducted through eigenvalue analysis. The stability analysis under control saturation is also treated in Section III using the so-called absolute stability theory. Robust stability analysis is performed in Section IV to investigate the effect of parameter variations on both system stability and control performance. In Section V, numerical simulations are carried out to test and compare the performances of the proposed controller with those of PR controller combined capacitor current feedback. Experimental test results are presented in Section VI considering several scenarios. Finally, Section VII concludes this article.

II. Design of the Composite Controller

A. System Model

In the stationary reference frame, the model of the LCL filter can be expressed as

$$\begin{aligned}\dot{x}_\alpha &= Ax_\alpha + B_u u_\alpha + B_v v_{g\alpha}\\ \dot{x}_\beta &= Ax_\beta + B_u u_\beta + B_v v_{g\beta}\end{aligned} \tag{1}$$

where

$$x_\alpha = \begin{bmatrix} i_{c\alpha} & v_{c\alpha} & i_{g\alpha}\end{bmatrix}^T, \quad x_\beta = \begin{bmatrix} i_{c\beta} & v_{c\beta} & i_{g\beta}\end{bmatrix}^T. \tag{2}$$

Here, $i_{c\alpha}$ and $i_{c\beta}$ are the $\alpha-\beta$-axis components of the converter current i_c. $v_{c\alpha}$ and $v_{c\beta}$ are the $\alpha-\beta$-axis components of the capacitor voltage v_c. $i_{g\alpha}$ and $i_{g\beta}$ are the $\alpha-\beta$-axis components of the grid current. The control inputs u_α and u_β represent the $\alpha-\beta$-axis components of voltage u at the output of the inverter, while $v_{g\alpha}$ and $v_{g\beta}$ represent the $\alpha-\beta$-axis components of the grid voltage v_g. The matrices A, B_u, and B_v are given by

$$A = \begin{bmatrix} 0 & -\frac{1}{L_c} & 0\\ \frac{1}{C_f} & 0 & -\frac{1}{C_f}\\ 0 & \frac{1}{L_g} & 0\end{bmatrix}, \quad B_u = \begin{bmatrix}\frac{1}{L_c}\\ 0\\ 0\end{bmatrix} \tag{3}$$

and

$$B_v = \begin{bmatrix} 0\\ 0\\ -\frac{1}{L_g}\end{bmatrix} \tag{4}$$

where L_c, C_f, and L_g are the converter-side inductance, filter capacitor, and grid-side inductance, respectively. As can be concluded from (1), $\dot{x}_\alpha$-equation and $\dot{x}_\beta$-equation are decoupled and have the same dynamics. Driven by this observation, a current controller can be designed by considering only either $\dot{x}_\alpha$-equation or $\dot{x}_\beta$-equation. This can be achieved by omitting the subscript $\alpha\beta$ in (1), yielding

$$\dot{x} = Ax + B_u u + B_v v_g. \tag{5}$$

To account for model uncertainties, (5) can be rewritten as

$$\dot{x} = Ax + B_u u + B_v v_g + B_b b. \tag{6}$$

To ease the control design, it is assumed that the matrix $B_b \in \mathbb{R}^{3\times 3}$ is diagonal, i.e.,

$$B_b = \begin{bmatrix}\frac{1}{L_c} & 0 & 0\\ 0 & \frac{1}{C_f} & 0\\ 0 & 0 & \frac{1}{L_g}\end{bmatrix}. \tag{7}$$

As in [37], the disturbance $b \in \mathbb{R}^3$ is assumed to oscillate at the fundamental frequency ω_f, i.e.,

$$b = \begin{bmatrix} b_1\\ b_2\\ b_3\end{bmatrix} = \begin{bmatrix} b_{M1}\cos(\omega_f t + \varphi_1)\\ b_{M2}\cos(\omega_f t + \varphi_2)\\ b_{M3}\cos(\omega_f t + \varphi_3)\end{bmatrix} \tag{8}$$

where the amplitude $b_{M\{1,2,3\}}$ and the phase $\varphi_{\{1,2,3\}}$ are not known; only ω_f is assumed to be known. The main objective of this work is to design a current controller that can ensure stable, robust, and accurate regulation of the grid current i_g. Such a control objective can be achieved using the following perturbed linear state model:

$$\begin{aligned}\dot{x} &= Ax + B_u u + B_v v_g + B_b b\\ y &= i_g = Cx\end{aligned} \tag{9}$$

where

$$C = \begin{bmatrix} 0 & 0 & 1\end{bmatrix}. \tag{10}$$

B. Design of the State-Feedback Controller

In this work, all states are assumed to be available for feedback. In addition, by assuming that all disturbance inputs are measurable, a simple state-feedback controller can be used to design a stable control for the system (6)–(8). With a view to reduce the design complexity, the feedback linearization approach can be used as a design procedure even if the system under study is linear. The main reason for choosing such a design procedure is that it provides a systematic way to select all control gains considering the performance specifications. Such a control design requires computing the relative degree of the system (9). To this end, it can be easily verified that

$$CB_u = 0, \quad CAB_u = 0, \quad CA^2B_u \neq 0 \tag{11}$$

which implies that the system (9) has relative degree three, which is equal to the system's order. Therefore, following [38], the system (9) does not have zero dynamics, and a simple feedback linearization technique can be used as a design procedure to develop a stable current controller for the system under study. In particular, following [38], the feedback linearization technique can be applied to design a state-feedback controller such that the closed-loop system is represented by

$$\dddot{e} + k_2\ddot{e} + k_1\dot{e} + k_0 e = 0 \tag{12}$$

where $e = y_r - y$ is the tracking error between the grid current i_g and its reference signal i_{gref}, with $y_r = i_{gref}$ and $y = i_g$. The control gains k_0, k_1, and k_2 can be tuned considering the desired transient response. Following [38], it can be shown that the above error equation can be obtained with the following state-feedback control law:

$$\begin{aligned} u = & -G^{-1}\left(K_x x + K_r y_r + K_{dr}\dot{y}_r + K_v v_g + K_{dv}\dot{v}_g\right) \\ & - G^{-1}\left(K_b b + K_{db}\dot{b}\right) \end{aligned} \tag{13}$$

where

$$\begin{aligned} G &= CA^2B_u, \quad K_x = k_0 C + DA \\ K_r &= -\left(k_0 - k_2\omega_f^2\right), \quad K_{dr} = -\left(k_1 - \omega_f^2\right) \end{aligned} \tag{14}$$

and

$$\begin{aligned} K_v &= DB_v - \omega_f^2 CB_v, \quad K_{dv} = k_2 CB_v + CAB_v \\ K_b &= DB_b - \omega_f^2 CB_b, \quad K_{db} = k_2 CB_b + CAB_b. \end{aligned} \tag{15}$$

The matrix D is given by

$$D = k_1 C + k_2 CA + CA^2. \tag{16}$$

Clearly, the parameters of the controller (13)–(16) can be calculated using the nominal values of the LCL filter and the control gains $k_{\{0:2\}}$. From (12), it follows that $k_{\{0:2\}}$ can be selected based on the desired closed-loop poles s_0, s_1, and s_2. As in [39], the closed-loop poles can be selected as

$$s_0 = -k, \qquad s_{1,2} = -\zeta\omega_n \pm j\omega_n\sqrt{1-\zeta^2}. \tag{17}$$

According to [39], the damping ratio ζ is restricted to $0.05 < \zeta < 0.3$, while the natural frequency ω_n can be set to be equal to the resonance frequency ω_r of the LCL filter, i.e.,

$$\omega_n = \omega_r = \sqrt{(L_c + L_g)/L_c L_g C_f}. \tag{18}$$

The positive constant k can be chosen as large as possible to ensure fast transient response. Had the closed-loop poles been selected, the control gains could have been calculated using the characteristic equation

$$(s - s_0)(s - s_1)(s - s_2) = s^3 + k_2 s^2 + k_1 s + k_0 \tag{19}$$

which leads to

$$k_0 = k\omega_n^2, \quad k_1 = 2k\zeta\omega_n + \omega_n^2, \quad k_2 = 2\zeta\omega_n + k. \tag{20}$$

The implementation of the control law (13) requires the variables b and $\dot{b}$ to be known, which is not possible by direct measurement. To overcome such a problem, the variable b and $\dot{b}$ in (13) can be replaced by their estimates $\hat{b}$ and $\dot{\hat{b}}$, respectively. That is

$$\begin{aligned} u = & -G^{-1}\left(K_x x + K_r y_r + K_{dr}\dot{y}_r + K_v v_g + K_{dv}\dot{v}_g\right) \\ & - G^{-1}\left(K_b \hat{b} + K_{db}\dot{\hat{b}}\right). \end{aligned} \tag{21}$$

Thus, the difficulty in measuring the disturbance b and its time derivative $\dot{b}$ can be overcome by designing a disturbance observer to estimate $\hat{b}$ and $\dot{\hat{b}}$.

C. Design of the Disturbance Observer

Let m be a positive integer such that $m = \{1, 2, 3\}$, therefore, from (8), it follows that:

$$\dot{b}_m = -\omega_f b_{Mm}\sin\left(\omega_f t + \varphi_m\right). \tag{22}$$

Let $\vartheta = [\vartheta_1 \quad \vartheta_2 \quad \vartheta_3]^T$ be an auxiliary disturbance input such that

$$\vartheta_m = -\omega_f b_{Mm}\sin\left(\omega_f t + \varphi_m\right) \tag{23}$$

for all m. Therefore, it is easy to see that

$$\begin{aligned} \dot{b}_m &= \vartheta_m \\ \dot{\vartheta}_m &= -\omega_f^2 b_m \end{aligned} \tag{24}$$

for all m. Recall that all state variables are assumed to be available for feedback. In addition, (7) and (8) indicates that each disturbance b_m enters only one state equation; b_1 enter $\dot{i}_c$-equation, b_2 enter $\dot{v}_c$-equation, and b_3 enter $\dot{i}_g$-equation. Driven by this observation, three independent observers can be developed to estimate the unknown disturbances b_1, b_2, and b_3; each observer uses only one state equation. That is, the observer for b_1 can take the form

$$\begin{aligned} \dot{\hat{i}}_c &= \frac{1}{L_c}u - \frac{1}{L_c}v_c + \frac{1}{L_c}\hat{b}_1 + N_1\left(\hat{i}_c - i_c\right) \\ \dot{\hat{b}}_1 &= \hat{\vartheta}_1 + L_c N_2\left(\hat{i}_c - i_c\right) \\ \dot{\hat{\vartheta}}_1 &= -\omega_f^2\hat{b}_1 + L_c N_3\left(\hat{i}_c - i_c\right) \end{aligned} \tag{25}$$

where $\hat{i}_c$, $\hat{b}_1$, and $\hat{\vartheta}_1$ are the estimates of i_c, b_1, and ϑ_1, respectively. The observer gains N_1, N_2, and N_3 should be selected based on the stability condition of the observer (25). Indeed, by setting $\sigma_1 = [i_c \quad b_1 \quad \vartheta_1]^T$, it can be shown that the estimation error $e_\sigma = \hat{\sigma}_1 - \sigma_1$ is governed by

$$\dot{e}_\sigma = \dot{\hat{\sigma}}_1 - \dot{\sigma}_1 = \Omega_{cl} e_\sigma \tag{26}$$

where

$$\Omega_{cl} = \begin{bmatrix} N_1 & \frac{1}{L_c} & 0 \\ L_c N_2 & 0 & 1 \\ L_c N_3 & -\omega_f^2 & 0 \end{bmatrix}. \tag{27}$$

Equations (26) and (27) indicates that the observer (25) can be made stable by selecting the gains $N_{\{1:3\}}$ such that the eigenvalues of the matrix Ω_{cl} are located in the open left-half plane. In particular, the matrix Ω_{cl} can be designed to have multiple eigenvalues at $-1/\varepsilon$, with ε is a positive constant. It can be verified that such a specific location of the observer eigenvalues can be achieved by choosing the observer gains $N_{\{1:3\}}$ as

$$N_1 = -\frac{3}{\varepsilon}, \quad N_2 = -\frac{3}{\varepsilon^2}\left(1 - \varepsilon^2\frac{\omega_f^2}{3}\right) \tag{28}$$

and

$$N_3 = -\frac{1}{\varepsilon^3}\left(1 - 3\varepsilon^2\omega_f^2\right). \tag{29}$$

By proceeding in the same manner, one can use $\dot{v}_c$-equation and $\dot{i}_g$-equation to construct estimators for $\hat{b}_2$ and $\hat{b}_3$. That is

$$\begin{aligned}\dot{\hat{v}}_c &= \frac{1}{C_f}i_c - \frac{1}{C_f}i_g + \frac{1}{C_f}\hat{b}_2 + N_4\left(\hat{v}_c - v_c\right)\\ \dot{\hat{b}}_2 &= \hat{\vartheta}_2 + C_f N_5\left(\hat{v}_c - v_c\right)\\ \dot{\hat{\vartheta}}_2 &= -\omega_f^2\hat{b}_2 + C_f N_6\left(\hat{v}_c - v_c\right)\end{aligned} \tag{30}$$

and

$$\begin{aligned}\dot{\hat{i}}_g &= \frac{1}{L_g}v_c - \frac{1}{L_g}v_g + \frac{1}{L_g}\hat{b}_3 + N_7\left(\hat{i}_g - i_g\right)\\ \dot{\hat{b}}_3 &= \hat{\vartheta}_3 + L_g N_8\left(\hat{i}_g - i_g\right)\\ \dot{\hat{\vartheta}}_3 &= -\omega_f^2\hat{b}_3 + L_g N_9\left(\hat{i}_g - i_g\right).\end{aligned} \tag{31}$$

As before, the above observers can be designed to have multiple eigenvalues at $-1/\varepsilon$ by setting the observer gains $N_{\{4:9\}}$ as

$$\begin{aligned}N_4 &= N_7 = N_1\\ N_5 &= N_8 = N_2\\ N_6 &= N_9 = N_3.\end{aligned} \tag{32}$$

Remark 1: The expressions of the gains $N_{\{1:9\}}$ indicate that the proposed disturbance observer belongs to high-gain observer approach [40]. When the three observers are put together, the resulting observer will have nine eigenvalues at $-1/\varepsilon$. Therefore, the estimation error can be made to vanish rapidly by choosing ε sufficiently small. However, in practice, a too small value of ε would magnify the effect of measurement noise. Therefore, real-time implementation of the developed observers involves careful choice of the value of ε.

Had the observers for both $\hat{b}$ and $\hat{\vartheta}$ been designed, the feedback controller (21) could have been implemented by setting $\dot{\hat{b}} = \hat{\vartheta}$, yielding

$$\begin{aligned}u = &-G^{-1}\left(K_x x + K_r y_r + K_{dr}\dot{y}_r + K_v v_g + K_{dv}\dot{v}_g\right)\\ &-G^{-1}\left(K_b\hat{b} + K_{db}\hat{\vartheta}\right).\end{aligned} \tag{33}$$

Remark 2: The grid current reference y_r may be generated by an outer loop, meaning that y_r can be expressed as a function of the measurement. Therefore, calculating $\dot{y}_r$ and $\dot{v}_g$ for the implementation of (33) can raise a concern about magnification of the effect of measurement noise. Therefore, lack of measurement of $\dot{y}_r$ and $\dot{v}_g$ can create difficulties in implementing (33) in practice. This problem is solved in this article by modifying the disturbance observer (25) to implicitly compensate for the terms $\dot{y}_r$ and $\dot{v}_g$.

D. Composite Controller for Real-Time Implementation

In practice, the control input can exceed its maximal value during transients, i.e., the duty cycle can go above the unity. This problem is generally addressed in practice by limiting the control input during transients through the use of a saturation block. Thus, the $\dot{\hat{i}}_c$-equation of the disturbance observer (25) can be rewritten as

$$\dot{\hat{i}}_c = \frac{1}{L_c}u_M sat\left(\frac{u}{u_M}\right) - \frac{1}{L_c}v_c + \frac{1}{L_c}\hat{b}_1 + N_1\left(\hat{i}_c - i_c\right) \tag{34}$$

where

$$sat\left(\frac{u}{u_M}\right) = \begin{cases} sign\left(\dfrac{u}{u_M}\right), & |u| > u_M\\ \dfrac{u}{u_M}, & |u| < u_M.\end{cases} \tag{35}$$

Here, u_M is the maximum peak voltage that can be produced at the output of the inverter. The above $\dot{\hat{i}}_c$-equation can be rewritten as

$$\dot{\hat{i}}_c = \frac{1}{L_c}u - \frac{1}{L_c}\Delta u - \frac{1}{L_c}v_c + \frac{1}{L_c}\hat{b}_1 + N_1\left(\hat{i}_c - i_c\right) \tag{36}$$

where

$$\Delta u = u - u_M sat\left(\frac{u}{u_M}\right). \tag{37}$$

The nonlinear function Δu is known as dead-zone function. Now, substituting (33) into (36) results in

$$\begin{aligned}\dot{\hat{i}}_c = &-\frac{1}{L_c}G^{-1}\left(K_{dr}\dot{y}_r + K_{dv}\dot{v}_g\right)\\ &-\frac{1}{L_c}G^{-1}\left(K_x x + K_r y_r + K_v v_g + K_b\hat{b} + K_{db}\hat{\vartheta}\right)\\ &-\frac{1}{L_c}\Delta u - \frac{1}{L_c}v_c + \frac{1}{L_c}\hat{b}_1 + N_1\left(\hat{i}_c - i_c\right).\end{aligned} \tag{38}$$

The implementation of (38) requires the information about $\dot{y}_r$ and $\dot{v}_g$, which are not always available for direct measurement. To tackle the need for $\dot{y}_r$ and $\dot{v}_g$, one can introduce a new state variable $\hat{\xi} \in \mathbb{R}$ such that

$$\hat{\xi} = \hat{i}_c + \frac{1}{L_c}G^{-1}\left(K_{dr}y_r + K_{dv}v_g\right). \tag{39}$$

Therefore, (38) can be implemented as

$$\begin{aligned}\dot{\hat{\xi}} = &-\frac{1}{L_c}G^{-1}\left(K_x x + K_r y_r + K_v v_g + K_b\hat{b} + K_{db}\hat{\vartheta}\right)\\ &-\frac{1}{L_c}v_c + \frac{1}{L_c}\hat{b}_1 + N_1\left(\hat{i}_c - i_c\right) - \frac{1}{L_c}\Delta u\\ \hat{i}_c = &\hat{\xi} - \frac{1}{L_c}G^{-1}\left(K_{dr}y_r + K_{dv}v_g\right).\end{aligned} \tag{40}$$

The $\dot{\hat{\xi}}$-equation can be further simplified to

$$\begin{aligned}\dot{\hat{\xi}} = &N_1\hat{\xi} + \frac{1}{L_c}\hat{b}_1 - \frac{1}{L_c}G^{-1}\left(K_b\hat{b} + K_{db}\hat{\vartheta}\right)\\ &-\frac{1}{L_c}G^{-1}K_x x - N_1 i_c - \frac{1}{L_c}v_c - \frac{1}{L_c}\Delta u\\ &-\frac{1}{L_c}G^{-1}\left(\left(K_r + N_1K_{dr}\right)y_r + \left(K_v + N_1K_{dv}\right)v_g\right).\end{aligned} \tag{41}$$

In a similar way, the change of the variable (39) can be used to transform the $\dot{b}_1$-equation and $\dot{\vartheta}_1$-equation of the disturbance

observer (25) into

$$\begin{aligned}\dot{\hat{b}}_1 &= L_cN_2\hat{\xi} + \hat{\vartheta}_1 - L_cN_2i_c - N_2G^{-1}K_{dr}y_r \\ &\quad - N_2G^{-1}K_{dv}v_g \\ \dot{\hat{\vartheta}}_1 &= L_cN_3\hat{\xi} - \omega_f^2\hat{b}_1 - L_cN_3i_c - N_3G^{-1}K_{dr}y_r \\ &\quad - N_3G^{-1}K_{dv}v_g. \end{aligned} \tag{42}$$

The state equations (41) and (42) can be rewritten in a compact form. Toward this end, define a new state variable $z \in \mathbb{R}^9$ such that

$$z = \begin{bmatrix} z_1^T & z_2^T & z_3^T \end{bmatrix}^T \tag{43}$$

where $z_1 \in \mathbb{R}^3$, $z_2 \in \mathbb{R}^3$, and $z_3 \in \mathbb{R}^3$ are given by

$$z_1 = \begin{bmatrix} \xi & b_1 & \vartheta_1 \end{bmatrix}^T \tag{44}$$

and

$$z_2 = \begin{bmatrix} v_c & b_2 & \vartheta_2 \end{bmatrix}^T, \quad z_3 = \begin{bmatrix} i_g & b_3 & \vartheta_3 \end{bmatrix}^T. \tag{45}$$

Recall that $\hat{b} = [\hat{b}_1 \quad \hat{b}_2 \quad \hat{b}_3]^T$ and $\hat{\vartheta} = [\hat{\vartheta}_1 \quad \hat{\vartheta}_2 \quad \hat{\vartheta}_3]^T$; therefore, one can write

$$\hat{b} = H_b\hat{z}, \qquad \hat{\vartheta} = H_\vartheta\hat{z} \tag{46}$$

where

$$H_b = \begin{bmatrix} 0 & 1 & 0 & 0 & 0 & 0 & 0 & 0 & 0 \\ 0 & 0 & 0 & 0 & 1 & 0 & 0 & 0 & 0 \\ 0 & 0 & 0 & 0 & 0 & 0 & 0 & 1 & 0 \end{bmatrix} \tag{47}$$

and

$$H_\vartheta = \begin{bmatrix} 0 & 0 & 1 & 0 & 0 & 0 & 0 & 0 & 0 \\ 0 & 0 & 0 & 0 & 0 & 1 & 0 & 0 & 0 \\ 0 & 0 & 0 & 0 & 0 & 0 & 0 & 0 & 1 \end{bmatrix}. \tag{48}$$

Thus, using (44), the observer (41)–(42) can be rewritten in a compact form as

$$\dot{\hat{z}}_1 = A_{z1}\hat{z}_1 + A_{x1}x + K_{z1}\hat{z} + A_{r1}y_r + A_{v1}v_g + A_{\Delta 1}\Delta u \tag{49}$$

where

$$A_{z1} = \begin{bmatrix} N_1 & \dfrac{1}{L_c} & 0 \\ L_cN_2 & 0 & 1 \\ L_cN_3 & -\omega_f^2 & 0 \end{bmatrix}. \tag{50}$$

The matrix A_{x1} is given by

$$A_{x1} = \begin{bmatrix} -\dfrac{1}{L_c}G^{-1}K_x \\ 0_{1\times 3} \\ 0_{1\times 3} \end{bmatrix} + \begin{bmatrix} -N_1 & -\dfrac{1}{L_c} & 0 \\ -L_cN_2 & 0 & 0 \\ -L_cN_3 & 0 & 0 \end{bmatrix}. \tag{51}$$

The matrices A_{r1} and A_{v1} are given by

$$A_{r1} = \begin{bmatrix} -\dfrac{1}{L_c}G^{-1}\left(K_r + N_1K_{dr}\right) \\ -N_2G^{-1}K_{dr} \\ -N_3G^{-1}K_{dr} \end{bmatrix} \tag{52}$$

and

$$A_{v1} = \begin{bmatrix} -\dfrac{1}{L_c}G^{-1}\left(K_v + N_1K_{dv}\right) \\ -N_2G^{-1}K_{dv} \\ -N_3G^{-1}K_{dv} \end{bmatrix}. \tag{53}$$

The matrices $A_{\Delta 1}$ and K_{z1} are expressed as

$$A_{\Delta 1} = \begin{bmatrix} -\dfrac{1}{L_c} \\ 0 \\ 0 \end{bmatrix}, \qquad K_{z1} = \begin{bmatrix} K_z \\ 0_{1\times 9} \\ 0_{1\times 9} \end{bmatrix} \tag{54}$$

where

$$K_z = -\frac{G^{-1}}{L_c}\left(K_bH_b + K_{db}H_\vartheta\right). \tag{55}$$

In a similar way, the observers (30) and (31) can be rewritten in a compact form using the $\hat{z}$-coordinates. To this end, note that (30) is expressed without explicit presence of u, y_r, $\hat{z}_1$, $\hat{z}_3$, and v_g, which makes it easy to derive $\dot{z}_2$-equation. Therefore, using (45), the observer (30) can take the compact form

$$\dot{\hat{z}}_2 = A_{z2}\hat{z}_2 + A_{x2}x \tag{56}$$

where

$$A_{z2} = \begin{bmatrix} N_4 & \dfrac{1}{C_f} & 0 \\ C_fN_5 & 0 & 1 \\ C_fN_6 & -\omega_f^2 & 0 \end{bmatrix} \tag{57}$$

and

$$A_{x2} = \begin{bmatrix} \dfrac{1}{C_f} & -N_4 & -\dfrac{1}{C_f} \\ 0 & -C_fN_5 & 0 \\ 0 & -C_fN_6 & 0 \end{bmatrix}. \tag{58}$$

Proceeding as before, it can be observed that (31) is expressed without explicit presence of u, y_r, $\hat{z}_1$, and $\hat{z}_2$. Thus, considering (45), the observer (31) can be rewritten as

$$\dot{\hat{z}}_3 = A_{z3}\hat{z}_3 + A_{x3}x + A_{v3}v_g \tag{59}$$

where

$$A_{z3} = \begin{bmatrix} N_7 & \dfrac{1}{L_g} & 0 \\ L_gN_8 & 0 & 1 \\ L_gN_9 & -\omega_f^2 & 0 \end{bmatrix} \tag{60}$$

and

$$A_{x3} = \begin{bmatrix} 0 & \dfrac{1}{L_g} & -N_7 \\ 0 & 0 & -L_gN_8 \\ 0 & 0 & -L_gN_9 \end{bmatrix}, \quad A_{v3} = \begin{bmatrix} -\dfrac{1}{L_g} \\ 0 \\ 0 \end{bmatrix}. \tag{61}$$

The differential equations (49), (56), and (59) can be put together to have one state model for the disturbance observer. That is

$$\dot{\hat{z}} = A_z\hat{z} + A_xx + A_ry_r + A_vv_g + A_\Delta\Delta u \tag{62}$$

where

$$A_z = \begin{bmatrix} A_{z1} & 0_{3\times3} & 0_{3\times3} \\ 0_{3\times3} & A_{z2} & 0_{3\times3} \\ 0_{3\times3} & 0_{3\times3} & A_{z3} \end{bmatrix} + \begin{bmatrix} K_{z1} \\ 0_{3\times9} \\ 0_{3\times9} \end{bmatrix} \tag{63}$$

and

$$A_x = \begin{bmatrix} A_{x1} \\ A_{x2} \\ A_{x3} \end{bmatrix}, \quad A_r = \begin{bmatrix} A_{r1} \\ 0_{3\times1} \\ 0_{3\times1} \end{bmatrix}. \tag{64}$$

The remaining matrices are given by

$$A_v = \begin{bmatrix} A_{v1} \\ 0_{3\times1} \\ A_{v3} \end{bmatrix}, \quad A_\Delta = \begin{bmatrix} A_{\Delta1} \\ 0_{3\times1} \\ 0_{3\times1} \end{bmatrix}. \tag{65}$$

Since the control input is already considered in the state equation of the observer, then, the resulting observer (62)–(65) is able compensate for the terms $\dot{y}_r$ and $\dot{v}_g$. Therefore, one can neglect such terms in the implementation of the control law (33), resulting in

$$u = -G^{-1}\left(K_x x + K_r y_r + K_v v_g\right) + L_c K_z \hat{z} \tag{66}$$

which can be rewritten as

$$u = -K_{xx}x - K_{zz}\hat{z} - K_{rr}y_r - K_{vv}v_g \tag{67}$$

where

$$\begin{aligned} K_{xx} &= G^{-1}K_x, \quad K_{zz} = -L_c K_z \\ K_{rr} &= G^{-1}K_r, \quad K_{vv} = G^{-1}K_v. \end{aligned} \tag{68}$$

III. Stability Analysis of the Nominal Closed-Loop System

A. Nominal Closed-Loop System Under the Composite Controller

The developed composite controller, consisting of (62) and (66), can be treated as a linear dynamic state-feedback control. That is

$$\begin{aligned} \dot{\hat{z}} &= A_z\hat{z} + A_x x + A_r y_r + A_v v_g + A_\Delta \Delta u \\ u &= -K_{xx}x - K_{zz}\hat{z} - K_{rr}y_r - K_{vv}v_g \end{aligned} \tag{69}$$

where the term $[A_\Delta \Delta u]$ can be viewed as an antiwindup compensator to cancel the effect of the control saturation during transients. The state equation that describes the nominal closed-loop system can be obtained by substituting the controller (66) into the state model (9). Here, the word "nominal" refers to the use of the the nominal parameters to calculate the matrices of the state model (9). To account for the limitation of the control input during transients, state equation (9) can be rewritten as

$$\dot{x} = Ax + B_u u_M sat\left(\frac{u}{u_M}\right) + B_v v_g + B_b b \tag{70}$$

which can be rewritten as

$$\dot{x} = Ax + B_u u + B_v v_g + B_b b - B_u \Delta u. \tag{71}$$

Now, substituting (67) into (71) gives

$$\begin{aligned} \dot{x} = {} & \left(A - B_u K_{xx} x\right) x - B_u K_{zz}\hat{z} - B_u K_{rr} y_r \\ & - \left(B_u K_{vv} - B_v\right) v_g + B_b b - B_u \Delta u. \end{aligned} \tag{72}$$

The complete state model of the nominal closed-loop system can be obtained by considering the dynamics of $\hat{z}$, given by (62). To do so, let $\eta \in \mathbb{R}^{12}$ be a new state variable such that

$$\eta = \begin{bmatrix} x & \hat{z} \end{bmatrix}^T. \tag{73}$$

The nominal closed-loop system can be then represented by the $\dot{\eta}$-equation. That is, augmenting (72) with (62) yields

$$\dot{\eta} = A_{cl}\eta + B_{clr}y_r + B_{clv}v_g + B_{clb}b + B_{cl\Delta}\Delta u \tag{74}$$

where

$$A_{cl} = \begin{bmatrix} \left(A - B_u K_{xx}\right) & -B_u K_{zz} \\ A_x & A_z \end{bmatrix} \tag{75}$$

and

$$B_{clr} = \begin{bmatrix} -B_u K_{rr} \\ A_r \end{bmatrix}, \quad B_{clv} = \begin{bmatrix} B_v - B_u K_{vv} \\ A_v \end{bmatrix}. \tag{76}$$

The matrices B_{clb} and $B_{cl\Delta}$ are given by

$$B_{clb} = \begin{bmatrix} B_b \\ 0_{9\times3} \end{bmatrix}, \quad B_{cl\Delta} = \begin{bmatrix} -B_u \\ A_\Delta \end{bmatrix}. \tag{77}$$

B. Stability Analysis of the Nominal Closed-Loop System in the Absence of Saturation

In the absence of saturation, the term Δu can be removed from (74), which helps reduce the complexity of the stability analysis of the nominal closed-loop system. In such a case, the stability of the nominal closed-loop system can be investigated by studying the eigenvalues of the matrix A_{cl}, provided that b, y_r, and v_g are bounded. In practice, y_r and v_g are bounded, therefore, it is clear that if b is bounded, then the stability of the closed-loop system will be determined by the eigenvalues of A_{cl}. Recall, that the composite controller is simply a combination of a state-feedback controller with an observer. Therefore, by separation principle, one can conclude that the set of eigenvalues of A_{cl}, denoted here by λ_{cl}, are the union of the observer eigenvalues λ_{obs} and the poles $s_{\{0,1,2\}}$, given by (17). This conclusion can be verified numerically by computing the eigenvalues of the matrix A_{cl} using MATLAB Software. That is

$$\lambda_{cl} = \{s_0, s_1, s_2, \lambda_{\text{obs}}\} \tag{78}$$

where s_0, s_1, and s_2 are given by (17) and

$$\lambda_{\text{obs}} = \left\{-\frac{1}{\varepsilon}, -\frac{1}{\varepsilon}, -\frac{1}{\varepsilon}, -\frac{1}{\varepsilon}, -\frac{1}{\varepsilon}, -\frac{1}{\varepsilon}, -\frac{1}{\varepsilon}, -\frac{1}{\varepsilon}, -\frac{1}{\varepsilon}, -\frac{1}{\varepsilon}\right\}. \tag{79}$$

Equations (78) and (79) imply that the matrix A_{cl} is Hurwitz by design. Therefore, the nominal closed-loop system is stable by design, provided that b is bounded. Now, it remains to investigate the asymptotic stability of the nominal closed-loop system. Toward this end, recall that both the current reference y_r and the disturbance b are assumed to oscillate with the fundamental frequency ω_f. This means that both y_r and b satisfy the same linear state equation (24) whose eigenvalues are located at $\pm j\omega_f$.

Therefore, following [41], if the set of the eigenvalues of the matrix A_z includes $\pm j\omega_f$, then the controller (69) achieves asymptotic stability of the closed-loop system. Let λ_z be the set of eigenvalues of A_z. Mathematically, it can easily be verified that

$$\lambda_z = \left\{ N_1, \pm j\omega_f, -\frac{1}{\varepsilon}, -\frac{1}{\varepsilon}, -\frac{1}{\varepsilon}, -\frac{1}{\varepsilon}, -\frac{1}{\varepsilon}, -\frac{1}{\varepsilon} \right\} \tag{80}$$

with $N_1 < 0$ is given by (28). Therefore, it follows from [41] that the developed controller (69) can achieve the tasks of stabilization, asymptotic tracking of sinusoidal reference, and rejection of sinusoidal disturbances provided that the control saturation does not affect the closed-loop stability.

C. Stability Analysis of the Nominal Closed-Loop System in the Presence of Saturation

As before, the stability of the closed-loop system in the presence of saturation can be reduced to study the stability of (74) with $(y_r, v_g, b) = (0, 0, 0_{1\times 3})$, and $\Delta u \neq 0$. When it does so, the state equation (74) together with the expression of the control input (67) reduces to

$$\begin{aligned} \dot{\eta} &= A_{cl}\eta + B_{cl\Delta}\Delta u(u) \\ u &= F\eta \end{aligned} \tag{81}$$

where

$$F = -\begin{bmatrix} K_{xx} & K_{zz} \end{bmatrix}. \tag{82}$$

Given the Hurwitz property of A_{cl} by design, the transfer function $G_s(s)$ from the nonlinear function $\Delta u(u)$ to the control input u, defined by

$$G_s(s) = F(sI - A_{cl})^{-1}B_{cl\Delta} \tag{83}$$

is also Hurwitz, with s is the Laplace operator. It is worth mentioning that although G_s is Hurwitz, the stability analysis of the closed-loop system (81) is a challenging task because the function $\Delta u(u)$ is nonlinear. In other words, the Hurwitz property of $G(s)$ and A_{cl} is not sufficient to conclude about the stability of the closed-loop system under control saturation. Rather, rigorous stability analysis requires the use of nonlinear techniques such as Lyapunov stability theory. In this work, absolute stability results, derived from Lyapunov stability theory, are directly applied to (81) to conclude about the stability of the closed-loop system under control saturation [38, Ch. 7]. Toward this end, rewrite (81) as in [38, Ch. 7]

$$\begin{aligned} \dot{\eta} &= A_{cl}\eta + B_{cl\Delta}\Delta u \\ u &= F\eta \\ \Delta u &= -\psi(t,u) \end{aligned} \tag{84}$$

where

$$\psi(t,u) = -\Delta u = u_M sat\left(\frac{u}{u_M}\right) - u. \tag{85}$$

The use of the absolute stability results to investigate the stability of (84)–(85) requires the nonlinearity $\psi(t,u)$ to satisfy the so-called a sector condition [38, Ch. 6]. Towards this end, one can use graphical representation of $\psi(t,u)$ to show that [38, Ch. 9]

$$|\psi(t,u)| \leq \frac{\delta}{1+\delta}|u|, \qquad \forall |u| \leq u_M(1+\delta) \tag{86}$$

where $\delta > 0$. Let γ be a real number such that

$$\gamma = \frac{\delta}{1+\delta} \quad \Rightarrow \quad \delta = \frac{\gamma}{1-\gamma}. \tag{87}$$

According to [38, Ch. 6], inequality (86) together with (87) indicates that the nonlinearity $\psi(u)$ belongs to the sector $[-\gamma, \gamma]$ only on the set $U \in \mathbb{R}$

$$U = \{u \in \mathbb{R}; \quad |u| \leq u_M(1+\delta)\}. \tag{88}$$

Notice that with $\delta > 0$, γ satisfies $0 < \gamma < 1$. Since $G(s)$ is Hurwitz and $\psi(u)$ satisfies a sector condition on a finite interval, stability of the closed-loop system can easily be investigated by direct application of absolute stability results. In particular, it can be shown that the closed-loop system (84) together with (86)–(88) is absolutely stable with a finite domain if [38, Ch. 7]

$$\gamma < \frac{1}{\sigma_{\max}(G_s(j\omega))} \tag{89}$$

where ω is the frequency in rad/s and $\sigma_{\max}(G_s(j\omega))$ is the maximum singular value of the transfer function $G_s(s)$. Using Table I, one can obtain

$$\sigma_{\max}(G_s(j\omega)) = 1.00565. \tag{90}$$

From (87) together with (89)–(90), it follows that:

$$0 < \delta < \frac{1}{\sigma_{\max}(G_s(j\omega)) - 1} < 177. \tag{91}$$

Inequality (91) can be used in (88) to estimate the range of $|u|$ for which the closed-loop system can remain absolutely stable during control saturation, i.e.,

$$|u| < 178u_M. \tag{92}$$

Since $u < u_M$ in steady-state, one can conclude that the stability of the closed-loop system under control saturation is guaranteed for a large value of $|u|$. More importantly, it is worthwhile to note that the estimated range $|u| < 178u_M$ may be conservative. Hence, the upper bound on $|u|$ may be much bigger than $178u_M$. Therefore, one can arrive at the conclusion that the closed-loop system under the proposed controller can remain absolutely stable even during control saturation for a relatively large value of $|u|$.

TABLE I
FILTER PARAMETERS AND CONTROL PARAMETERS

Filter parameter	Values	Control parameters	Values
L_c	4.2 mH	k	1000
L_g	2.5 mH	ζ	0.17
C_f	8 μF	ε	0.0004
ω_r	8931.0 rd/s	ω_n	ω_r
ω_f	$2\pi 50$ rd/s	f_{sw}	5 kHz
$e_{g_{L-L}}$	120 V	f_s	10 kHz

IV. Numerical Analysis of the Stability and Robustness of the Proposed Controller in the Presence of Uncertain Parameters

A. Robust Stability to Parameter Variations

As pointed out above, the asymptotic stability of the closed-loop system requires the eigenvalues of the matrix A_{cl} to lie in the open left-half plane. This requirement can be met by the proposed design if the actual parameters coincide with the nominal ones, where the eigenvalues of A_{cl} can easily be assigned at desired locations. Nonetheless, if there is any difference between the system's parameters and their nominal values, the eigenvalues of the actual A_{cl} can move away from the desired locations, even migrate to the right-half plane. Robust stability to parametric uncertainty can be interpreted as a requirement that the eigenvalues of the uncertain A_{cl} remain in the left-half plane even though the actual system's parameters deviate from their nominal values. A rigorous analysis of the stability robustness to model uncertainties can be performed using the "Robust Control Toolbox" of MATLAB such as "μ Analysis and Synthesis Toolbox" [42]. In this work, the stability robustness to parameter variations is verified numerically by analyzing the eigenvalues of the uncertain matrix A_{cl} when L_c, C_f, and L_g are assumed to change by $\pm 50\%$. Toward this end, "Robust Control Toolbox" of MATLAB is used to create five uniformly spaced values of L_c, C_f, and L_g considering that the system's parameters change by $\pm 50\%$. This restriction on parameter changes is reasonable in view of the fact that these parameters are usually known with high precision for a properly designed *LCL* filter [8], and their values cannot exhibit large deviations from their nominal values. The obtained samples of these uncertain parameters are then exploited to create 125 samples of uncertain matrices A, B_u, B_v, and B_b that are required to build the uncertain state model (9). While the uncertain parameters are used to construct 125 samples of the uncertain state model, the proposed controller (69) is designed using only the nominal values. More precisely, the determined 125 samples of the uncertain matrices A and B_u are used in (75) to calculate the uncertain closed-loop matrix A_{cl}, with A_z, A_x, K_{zz}, and K_{xx} fixed at their nominal values. Fig. 2 shows the locations of the eigenvalues λ_{cl} that are obtained for 125 samples of uncertain A_{cl}, including the nominal A_{cl}. It can be seen from Fig. 2 that the closed-loop eigenvalues of all perturbed systems remain in the left-half plane, which demonstrates the robust stability of the proposed controller to the variation in the system's parameters.

B. Robustness of the Design Procedure to Parameter Variations

The locations of the nominal poles $s_{\{1,2\}}$ are selected to met the requirements $\omega_n = \omega_r$ and $0.05 < \zeta < 0.3$, where ω_n, ζ, and ω_r are the natural frequency of $s_{\{1,2\}}$, the damping ratio of $s_{\{1,2\}}$, and the resonance frequency of the *LCL* filter system. In the absence of model uncertainties, the requirement on ω_n and ζ can easily be met by using nominal parameters to assign the closed-loop poles $s_{\{1,2\}}$ at specific locations. The problem, however, is that parameters variations can cause the actual poles $s_{\{1,2\}}$ to change the locations in the complex plane, as can be seen from Fig. 2. This migration of closed-loop poles under model uncertainties raises a concern about the robustness of the design process and the validity of (18). To address this concern, Fig. 3 shows the behavior of the actual $s_{\{1,2\}}$ to the changes in the actual resonance frequency ω_r. The samples of ω_r and $s_{\{1,2\}}$ are directly calculated from 125 samples of uncertain parameters as before. The only difference between this test and the previous one is that the samples are created considering that the system's parameters change by $\pm 25\%$. It can be observed from Fig. 3 that the natural frequency ω_n of $s_{\{1,2\}}$, which is simply the magnitude of $s_{\{1,2\}}$, closely follows the actual resonance frequency ω_r despite changes in the system's parameters. This means that the requirement $\omega_n = \omega_r$ is almost satisfied for both nominal and perturbed systems under $\pm 25\%$ changes in system's parameters. What is also interesting is that the damping ratio ζ of $s_{\{1,2\}}$ remains within the interval $[0.05, 0.3]$ even in the presence of model uncertainties. The obtained results provides evidence to the robustness of the design process for a reasonable range of parameters variations [8]. The selected range of parameter

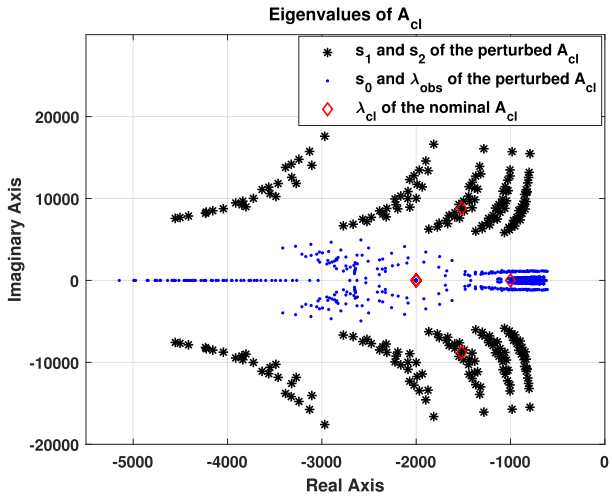

Fig. 2. Behavior of the closed-loop eigenvalues λ_{cl} in the presence of model uncertainties. 125 uncertain systems have been created by considering that the actual values of L_c, C_f, and L_g can change by $\pm 50\%$.

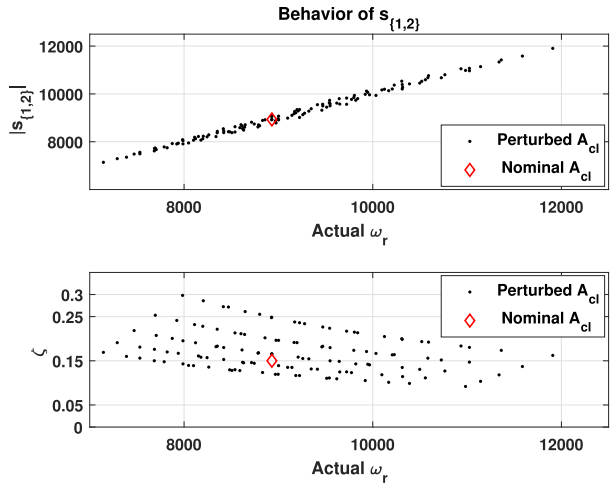

Fig. 3. Behavior of the uncertain closed-loop poles $s_{\{1,2\}}$ in terms of natural frequency ω_n and damping ratio ζ. 125 uncertain systems have been created by considering that the actual values of L_c, C_f, and L_g can change by $\pm 25\%$.

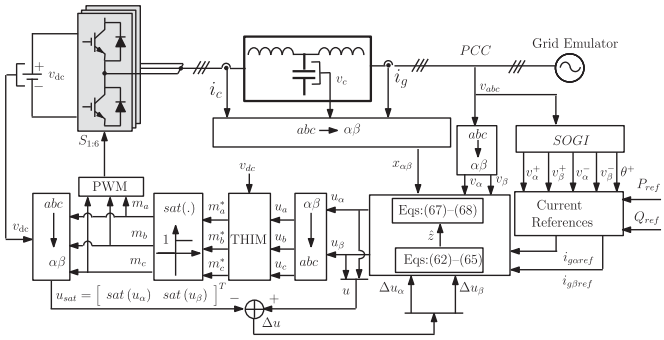

Fig. 4. Block diagram for testing the proposed controller. Here, THIM and SOGI stand for third harmonic injection method and second order generalized integrator (SOGI) algorithm [43], respectively.

variations to study the robustness of the design procedure should not undermine the ability of the proposed controller to provide good responses under a wide range of model uncertainty, as demonstrated in simulation and experimental tests.

V. Simulation Results

The preliminary testing of the proposed controller was performed by simulation tests using MATLAB/Simulink software. The MATLAB/Simulink model was constructed to implement the proposed controller as illustrated in the block diagram in Fig. 4. The parameters of the complete setup are listed in Table I, with the dc-link voltage is set as $v_{dc} = 250$ V. The control gains $k_{\{0,1,2\}}$ are calculated using (20), with the control parameters k, ζ, and ω_n are given in the Table I. The observer parameter ε can be chosen as small as possible to ensure a fast disturbance estimation. In practice, the value of ε is limited to a certain minimum value because of the possible magnification of the effect of measurement noise. In addition, the sampling frequency also imposes a limit on how small the value of ε could be. In practice, It was found that $\varepsilon = 0.0004$ can offer good transient and steady-state performances with a minor sensitivity to measurement noise. The summary of the control parameters are given in Table I.

A. Performance Evaluation Under Nominal Parameters

This test was conducted to verify the transient and steady-state performances of the developed controller under balanced grid voltages and nominal parameters. Toward this end, this test was conducted by applying step changes in the command active power P_{ref}, while the command reactive power Q_{ref} was kept null. The power command values are then transformed to command currents $i_{g\alpha ref}$ and $i_{g\beta ref}$ by exploiting the direct relationship between active/reactive power, grid current, and grid voltage. In this test, the command value for the active power was stepped up as $P_{ref} : 0 \rightarrow 1000 \rightarrow 1800$ W. The obtained results are given in Fig. 5. Fig. 5(a) shows that the actual currents $i_{g\alpha}$ and $i_{g\beta}$ asymptotically track their sinusoidal references $i_{g\alpha ref}$ and $i_{g\beta ref}$ with zero steady-state error. Furthermore, the transient response to changes in the command currents takes place with a short settling time and without overshot. Overall, the proposed controller was able to quickly and accurately adjust the actual currents to meet the power command values as could be

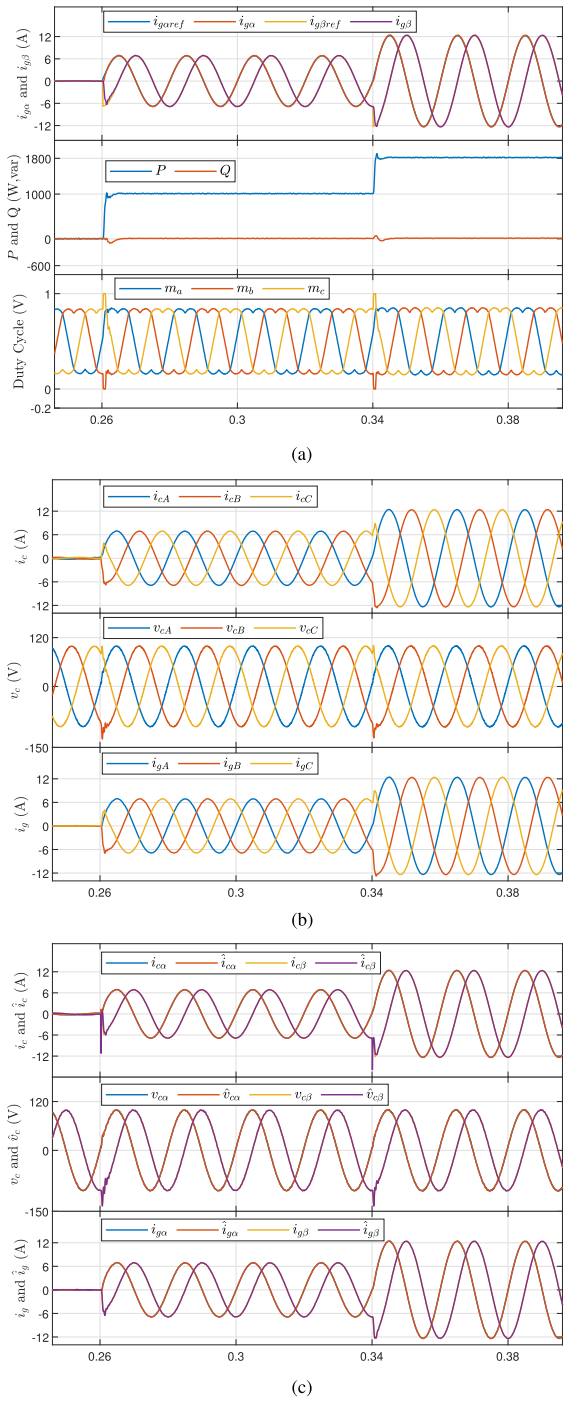

Fig. 5. Performance evaluation of the proposed controller in response to step changes in the active power considering balanced grid voltages and nominal parameters. (a) $\alpha\beta$-axis components of i_g and their references, active and reactive powers (P, Q), and modulating signals m_a, m_b, and m_c. (b) Converter-side current i_c, capacitor voltage v_c, and grid-side current i_g. (c) $\alpha\beta$-axis components of i_c, v_c, and i_g together with their estimates.

seen in Fig. 5(a). It can also be concluded from Fig. 5(b) that the proposed controller was able to operate the three-phase inverter to inject high quality currents into the grid as indicated by the sinusoidal waveforms of the currents i_c and i_g. To further investigate the performances of the developed controller, Fig. 5(c) also presents the measurements of $i_{g\{\alpha,\beta\}}$, $i_{c\{\alpha,\beta\}}$, and $v_{c\{\alpha,\beta\}}$ and their estimates $\hat{i}_{g\{\alpha,\beta\}}$, $\hat{i}_{c\{\alpha,\beta\}}$, and $\hat{v}_{c\{\alpha,\beta\}}$. The obtained

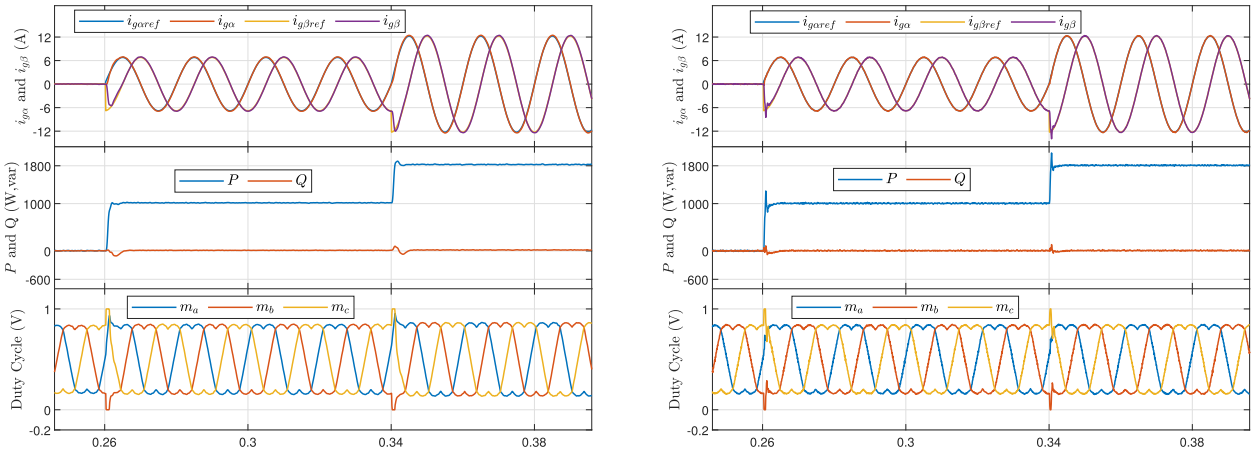

Fig. 6. Performance evaluation of the proposed controller in response to step changes in the active power considering balanced grid voltages and mismatch between the system's model and the actual system. (a) $\alpha\beta$-axis components of i_g and their references, active and reactive powers (P, Q), and modulating signals m_a, m_b, and m_c. These responses are obtained when the parameters of the actual system are set to be equal to 150% of their nominal values. (b) $\alpha\beta$-axis components of i_g and their references, active and reactive powers (P, Q), and modulating signals m_a, m_b, and m_c. These responses are obtained when the parameters of the actual system are set to be equal to 50% of their nominal values.

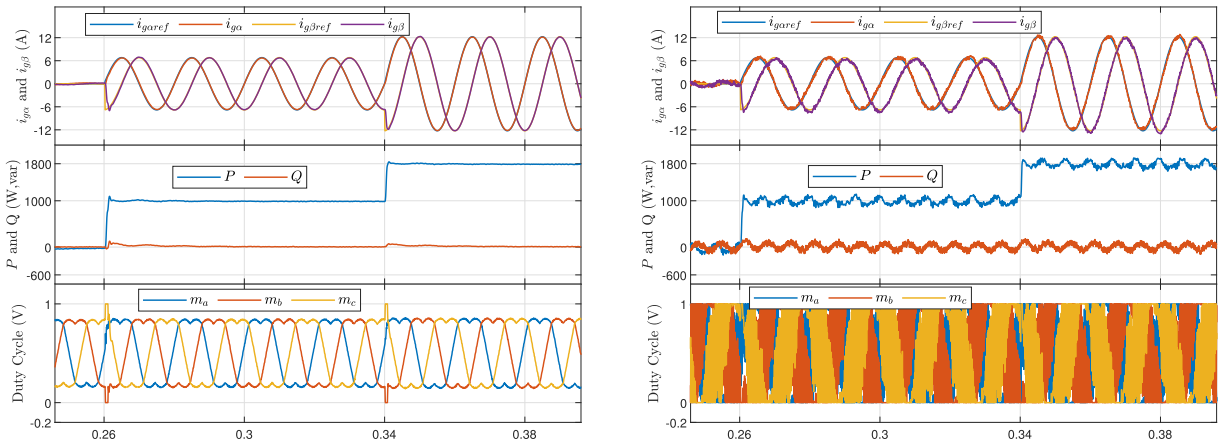

Fig. 7. Performance evaluation of the PR controller combined capacitor current feedback in response to step changes in the active power considering balanced grid voltages. The reference controller has been tested under both nominal and uncertain parameters. (a) $\alpha\beta$-axis components of i_g and their references, active and reactive powers (P, Q), and modulating signals m_a, m_b, and m_c. These responses are obtained under nominal parameters; there is no mismatch between the system's model and the actual system. (b) $\alpha\beta$-axis components of i_g and their references, active and reactive powers (P, Q), and modulating signals m_a, m_b, and m_c. These responses are obtained when the parameters of the actual system are set to be equal to 65% of their nominal values.

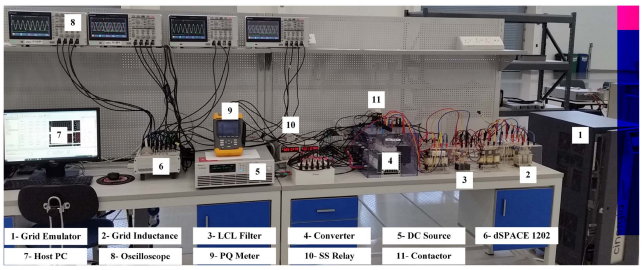

Fig. 8. Photograph of the laboratory setup for practical implementation of the proposed controller.

results show that the disturbance observer was fast, accurate and effective in estimating the actual measurement despite its sinusoidal nature, which provides evidence of the ability of the proposed controller to produce an accurate estimate of unknown disturbances. Another feature of the proposed controller is its ability to maintain good dynamic performances even if the modulating signals saturate during transients as could be seen from Fig. 5(a). This can be explained by the use of the term Δu in the control law, which can be viewed as an antiwindup scheme to attenuate the effect of control saturation during transients.

B. Performance Comparison Between the Proposed Controller and PR Controller Combined Capacitor Current Feedback Considering Uncertain Parameters

This test was conducted to verify the robustness of the developed controller to modeling errors. Another objective of

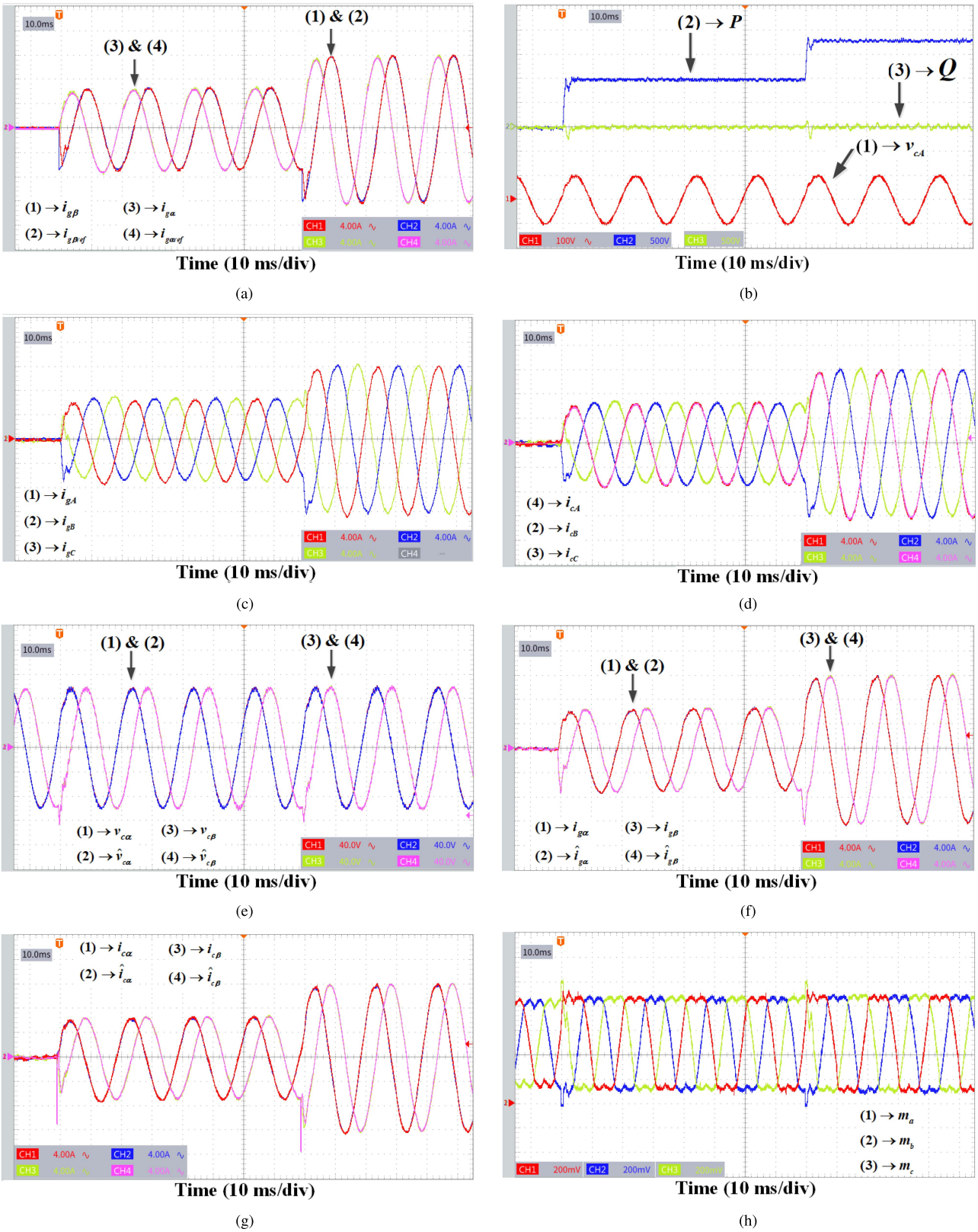

Fig. 9. Performance evaluation of the proposed controller under balanced grid voltages and in response to step changes in the active power. (a) $\alpha\beta$-axis components of i_g and their references. (b) Active and reactive powers (P, Q) and capacitor voltage v_{cA}. (c) Grid-side current i_g. (d) Converter-side current i_c. (e) $\alpha\beta$-axis components of v_c and their estimates. (f) $\alpha\beta$-axis components of i_g and their estimates. (g) $\alpha\beta$-axis components of i_c and their estimates. (h) Modulating signals m_a, m_b, and m_c.

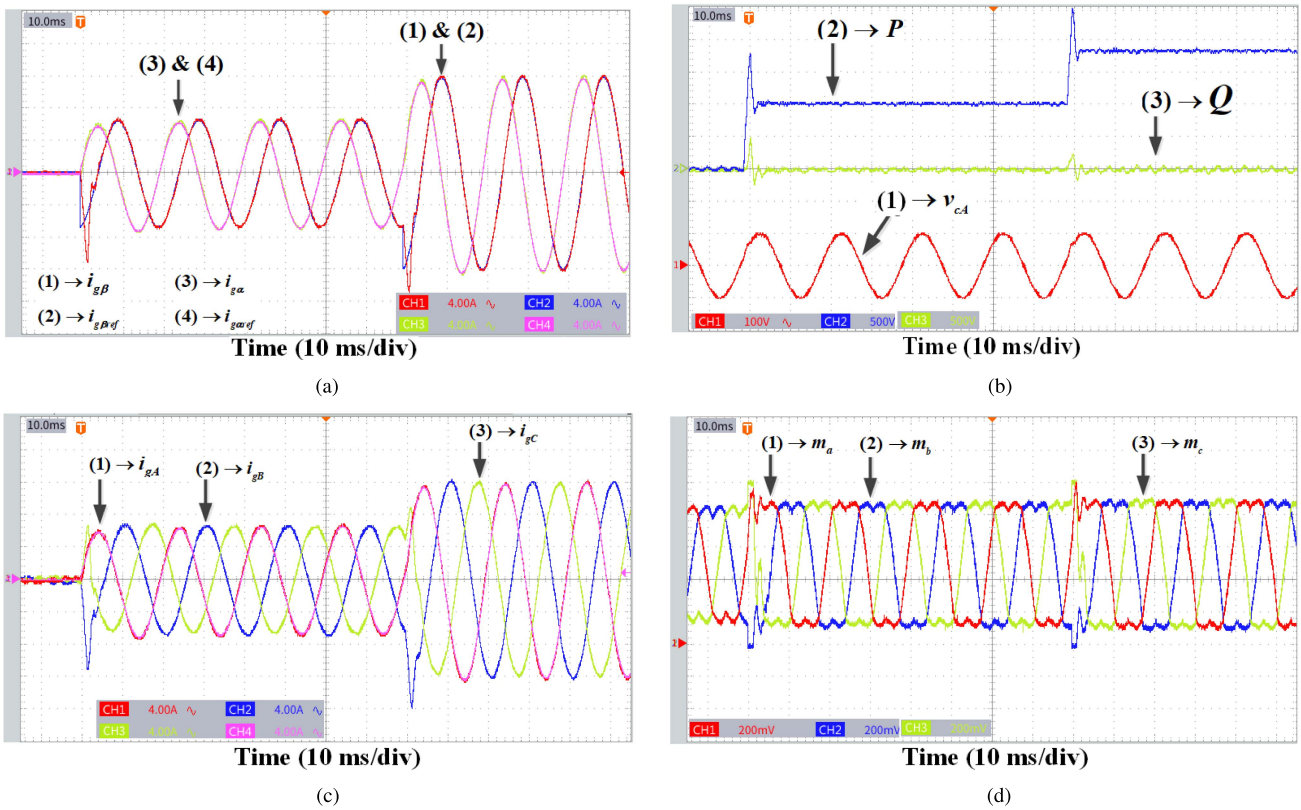

Fig. 10. Performance evaluation without the anti-windup feedback Δu in (62). (a) $\alpha\beta$-axis components of i_g and their references. (b) Active and reactive powers (P, Q) and capacitor voltage v_{cA}. (c) Grid-side current i_g. (d) Modulating signals m_a, m_b, and m_c.

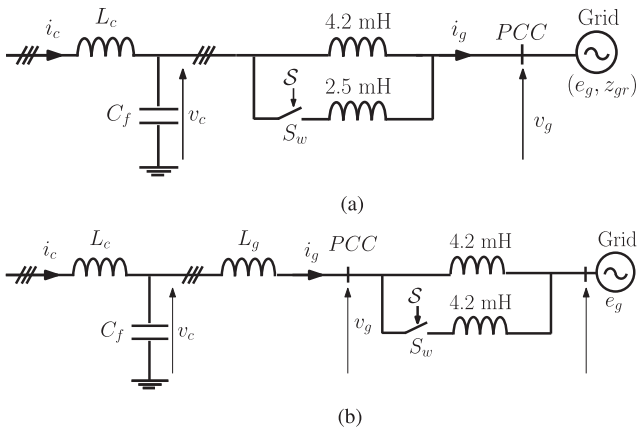

Fig. 11. Schematic diagrams for testing the proposed controller under parameters variations and weak grid. (a) Schematic diagram for emulating the changes in L_g. (b) Schematic diagram for emulating the changes in $Z_{gr} = L_{gr}$.

this test was to conduct a performance comparison between the proposed controller and PR controller which is one of the widely used control techniques. To this end, this test was carried out under the same conditions as those used in the previous one except that the system's model was created using incorrect parameters. More specifically, while the proposed controller was designed based on the nominal parameters, the system's model was constructed using incorrect parameters to emulate modeling errors. Moreover, to test the robustness of the proposed controller to different modeling errors, two test cases were conducted under the proposed controller as follows.

1) *Case A:* The system's model was constructed by considering that the system's parameters are 50% lower than the nominal parameters, which corresponds to an actual resonance frequency of $f_r = 2842.8$ Hz.
2) *Case B:* The system's model was created by considering that the system's parameters are 50% higher than the nominal parameters, which corresponds to an actual resonance frequency of $f_r = 947.6$ Hz.

To further highlight the advantages of the proposed controller, its performance is compared with the performance of PR controller as presented in [9]. The reference PR controller is also combined with the capacitor current feedback to damp down the effect of the resonant phenomenon, as presented in [9]. More information about the design and implementation of the PR controller combined capacitor current feedback can be found in Appendix. In this test, the PR controller was tested under both nominal parameters and uncertain parameters. Fig. 6 shows the results obtained with the proposed controller, while Fig. 7 shows the results obtained with the PR controller. The observed responses in Fig. 6(a) are found to be insensitive to $+50\%$ changes in the system's parameters. However, a small overshoot can be noticed in the transient responses when the system's parameters are 50% lower than the nominal parameters as shown in Fig. 6(b). Overall, the obtained results have revealed a negligible sensitivity of the proposed controller to changes in the system's parameters. More importantly, the variation in the

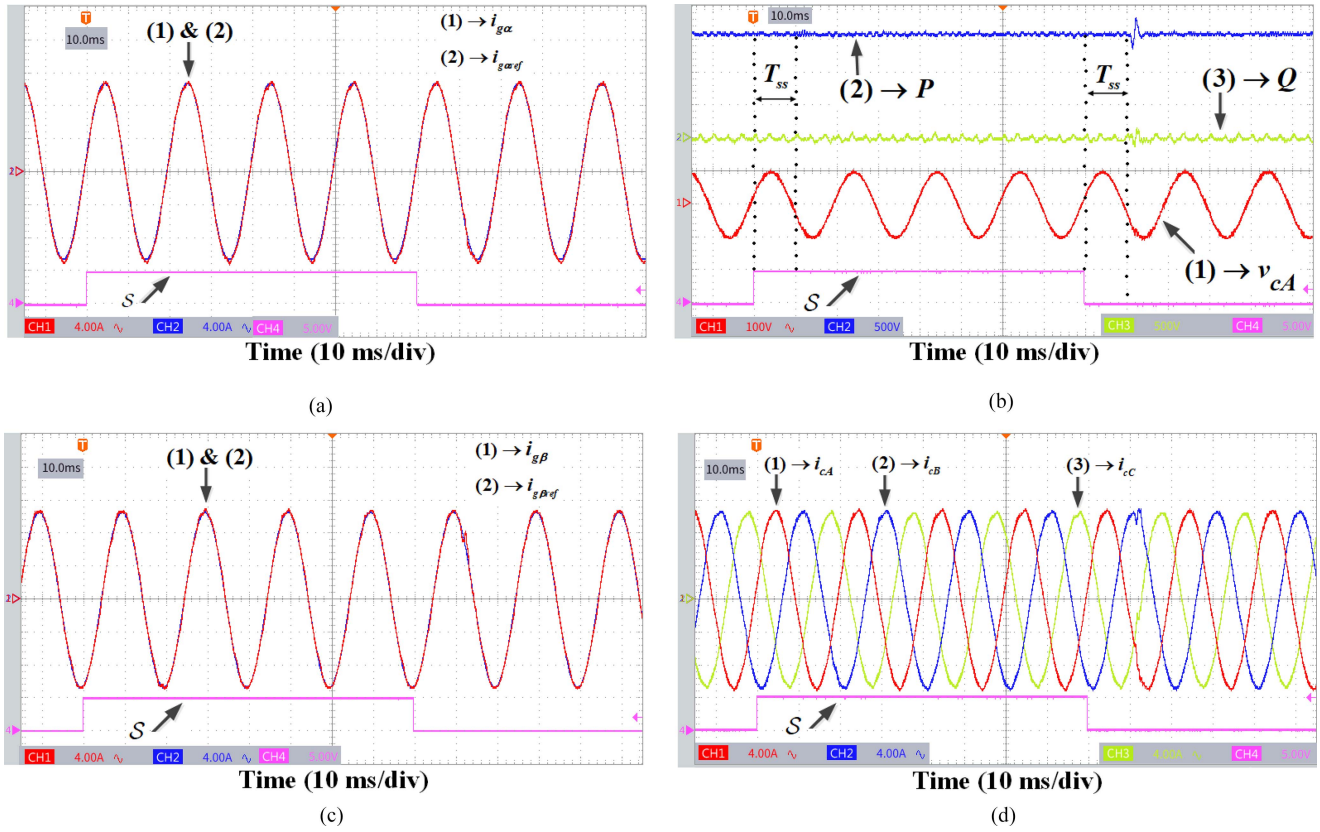

Fig. 12. Performance evaluation of the proposed controller under balanced grid voltages and in response to step changes in the grid-side inductance. Here, $\mathcal{S}$ is the command signal for the switch S_w which is used to change the actual value of L_g. T_{ss} is the delay of the switch; it is about 10 ms. (a) α-axis component of i_g and its reference. (b) Active and reactive powers (P, Q) and capacitor voltage v_{cA}. (c) β-axis component of i_g and its reference. (d) Converter-side current i_c.

system's parameters did not have any impact on the high quality of the grid currents, the modulating signals, and the active and reactive powers injected into the grid. The observed responses in Fig. 7(a) demonstrated the ability of the PR controller to initiate fast and accurate control of the grid current, particularly when the nominal parameters match the system's parameters. More importantly, the comparison between Figs. 5(a) and 7(a) shows some similarity in terms of transient responses; the responses under the PR controller approach the responses under the proposed controller. The observed responses under nominal parameters confirmed that the PR controller is well tuned to ensure a fair comparison with the proposed controller. The problem, however, is that the PR controller fails to maintain good steady-state performances when the system's parameters are only 35% lower than the nominal parameters, as can be seen from Fig. 7(b). More specifically, -35% changes in the system's parameters cause the closed-loop system under the PR controller to go unstable, as indicated by the behavior of the modulating signals. Overall, the performance comparison shows that proposed controller can outperform the conventional PR controller as the system's parameters change.

VI. Experimental Results

Experimental tests have been carried out to verify the performance of the proposed controller considering balanced voltages, unbalanced voltages, model uncertainties, and weak grid condition. The developed controller was implemented using dSPACE MicroLabBox (DS1202) as shown in Fig. 8. The setup for experimental testing of the proposed controller was composed of a dc power supply manufactured by Chroma, a Grid emulator manufactured by Cinergia, a three-phase inverter manufactured by Semikron, and a voltage and current input conditioning module manufactured by Oparl-rt. The nominal parameters of *LCL* filtered grid-tied VSI as well as the controller gains are exactly the same as those used in the simulation tests.

A. Performance Evaluation Under Balanced Grid Voltages

1) Performance Evaluation Under Nominal Parameters and Anti-Windup Feedback Δu: This test was conducted to confirm the simulation results for good dynamics and accuracy of the proposed controller in response to step changes in the active power injected into the grid. Toward this end, the conditions of this experiment were set to be exactly the same as those used for the first simulation test; i.e., when the controller is tested under nominal parameters. The results for this experiment are presented in Fig. 9. Comparing the responses of Fig. 9 with those of Fig. 5 shows that there is a close match between the simulation results and the experimental results. This consistency in responses between simulation and experimental tests provides another evidence to the effectiveness of the proposed controller.

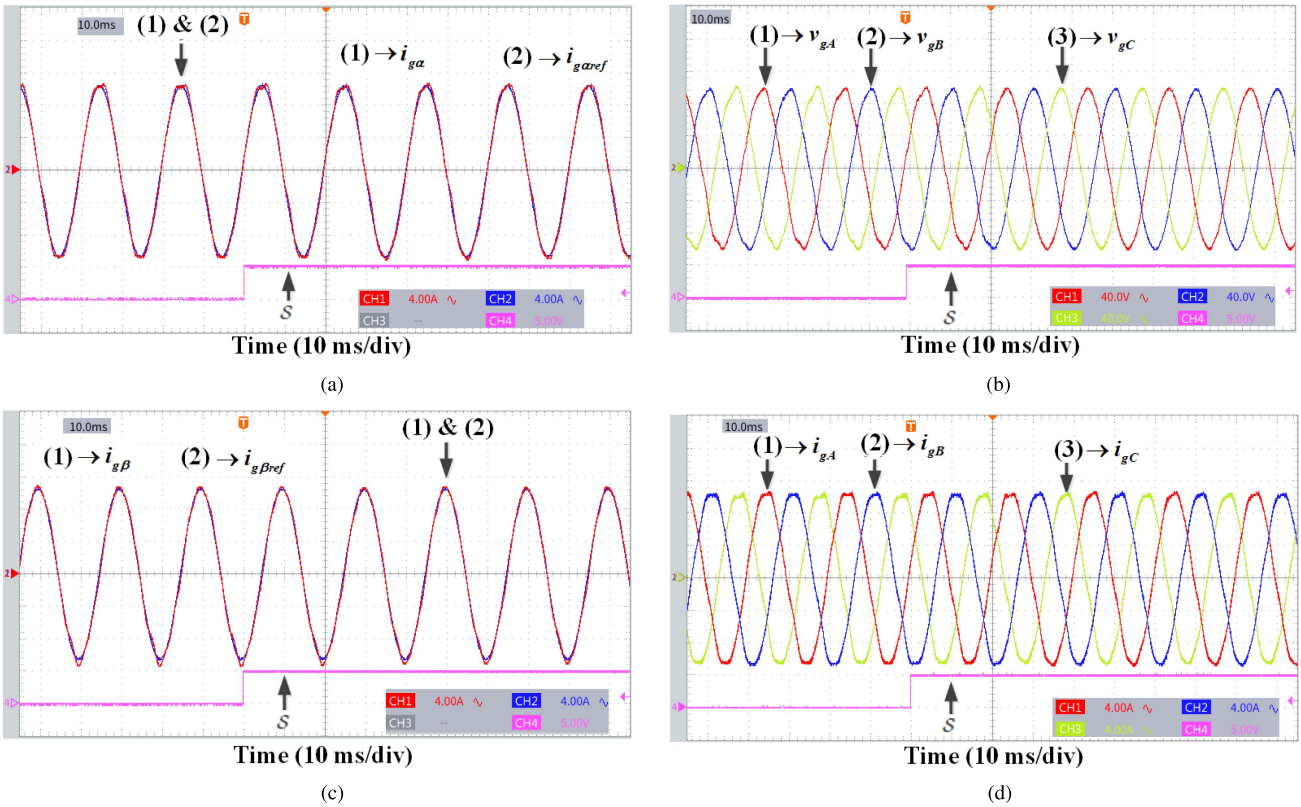

Fig. 13. Performance evaluation of the proposed controller under weak grid. Here, $\mathcal{S}$ is the command signal for activating and deactivating the switch S_w which is used to change the actual value of the grid impedance $Z_{gr} = L_{gr}$. (a) α-axis component of i_g and its reference. (b) Three-phase voltages v_g measured at the point of common coupling. (c) β-axis component of i_g and its reference. (d) Grid-side current i_g.

2) Performance Evaluation Under Nominal Parameters and Without Anti-Windup Feedback Δu: The objective of this test was to practically demonstrate the benefits of the anti-windup feedback Δu to mitigate the effect of the control saturation during transients. To this end, the conditions of this test were taken the same as in the previous test except that the antiwindup feedback is removed from the control scheme; i.e., Δu is set as $\Delta u = 0$ in (62). The results of this experiment are presented in Fig. 10. As shown in Fig. 10(a)–(c), the removal of the feedback Δu did not impact the steady-state performance of the composite controller, but, a large overshoot is observed during transients. This overshoot is mainly attributed to the buildup in the resonant controller during control saturation, as can be seen from Fig. 10(d). Comparing the responses of Fig. 9(a)–(c) and those of Fig. 10(a)–(c) reveals clearly the benefit and the contribution of the feedback Δu to maintain a graceful transient response during control saturation.

3) Performance Evaluation Under Changes in Grid-Side Inductance L_g: This test aims to evaluate the robustness of the proposed controller under parameter variations, which was achieved through real-time application of changes in the grid-side inductance L_g. Fig. 11(a) shows the schematic diagram for testing the controller under step changes in L_g. As can be seen from Fig. 11(a), the grid-side inductance was realized by connecting two inductors in parallel; the inductance values are 2.5 mH and 4.2 mH. The 2.5-mH inductance was connected to the grid via a solid-state switch S_w to allow changing the value of L_g in real-time. When the solid-state switch is activated, the value of L_g is simply the equivalent inductance of the two inductors in parallel, resulting in $L_g = 1.5672$ mH, but, when the solid-state switch is deactivated, the inductance L_g reduces to 4.2 mH. In other words, the actual inductance L_g can be either 1.5672 mH or 4.2 mH depending on the ON-OFF actions of the solid-state switch. To investigate the robustness of the proposed controller to model uncertainties, the control gains are calculated with $L_g = 2.8836$ mH which is considered as the nominal value for this test. With this nominal value of L_g, the robustness of the proposed controller can be tested to $\pm 45\%$ changes in the grid-side inductance by the ON-OFF switching of the solid-state switch. This test started with the deactivation of solid-state switch, i.e., with $L_g = 4.2$ mH. The experimental results for this test are shown in Fig. 12, from where it can be seen that the command signal $\mathcal{S}$ for the solid-state switch was changed as $\mathcal{S} : 0 \rightarrow 1 \rightarrow 0$. During this test, the three-phase inverter was controlled to feed the grid with 1600 W, which is achieved by setting $P_{ref} = 1600$ W and $Q_{ref} = 0$ var. Note that the solid-state switch has a delay of about 10 ms as could be seen from Fig. 12(b); this delay is denoted by T_{ss}. The results in Fig. 12 show that changes in L_g do not affect the stability of the closed-loop system, which confirms the theoretical analysis. Moreover, it can be observed that the obtained responses are almost insensitive to the step decrease in L_g, which is created by the ON action of the switch. On the other hand, it can be observed that the step increase in L_g caused the power response to slightly

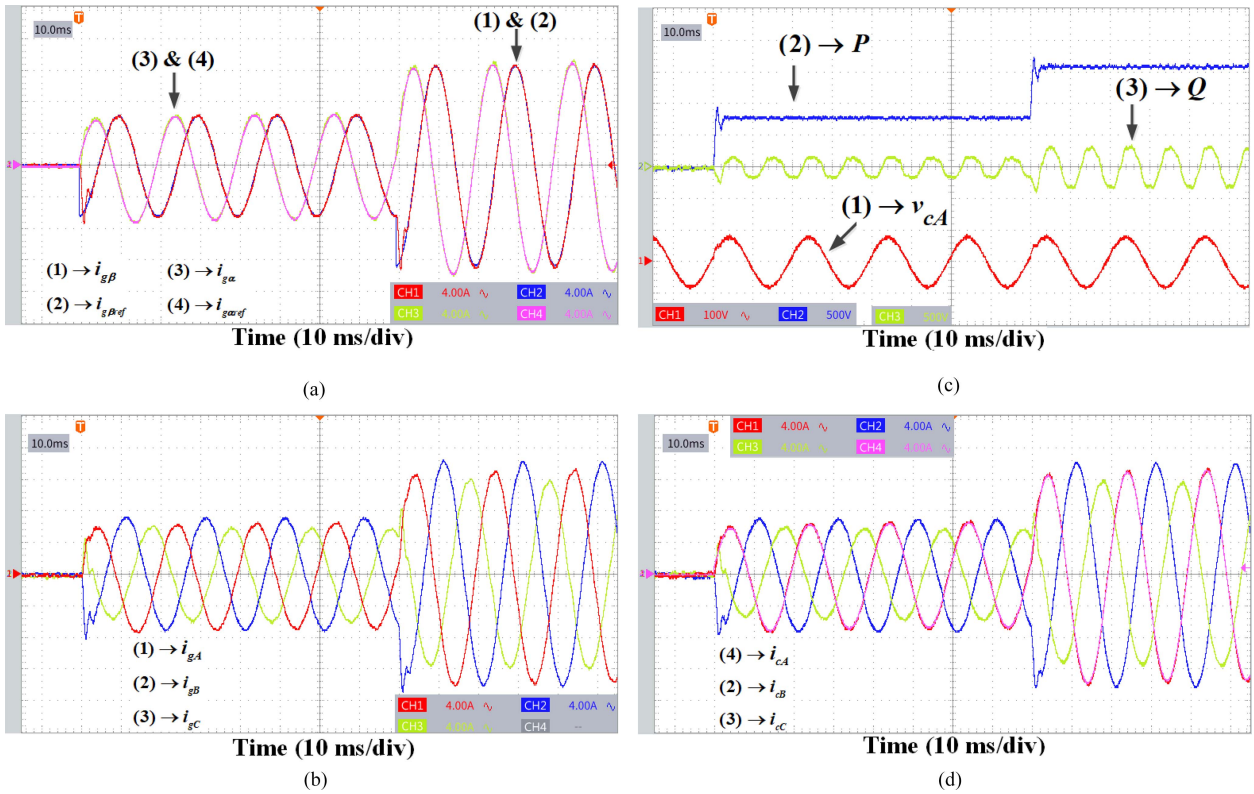

Fig. 14. Performance evaluation of the proposed controller under unbalanced grid voltages and in response to step changes in the active power. (a) $\alpha\beta$-axis components of i_g and their references. (b) Active and reactive powers (P, Q) and capacitor voltage v_{cA}. (c) Grid-side current i_g. (d) Converter-side current i_c.

deviate from its command value during a short transient period of about 4 ms, but, the power response was able to regain its steady-state conditions after the transient period has passed. Overall, observed responses demonstrated the ability of the developed controller to quickly compensate for the changes in L_g.

4) Performance Evaluation Under Changes in Grid inductance L_{gr}: For purposes of testing the proposed controller under a weak grid, this test was conducted under real-time application of changes in the grid impedance Z_{gr}. In this test, the grid impedance is represented by an inductance L_{gr}. Fig. 11(b) shows the schematic diagram for testing the controller under step changes in L_{gr}. As can be seen from Fig. 11(b), the grid inductance was realized by connecting two inductors in parallel; each inductance has a value of 4.2 mH. One of these inductors was connected to the grid via a solid-state switch S_w to allow changing the value of L_{gr} in real-time. The value of L_{gr} is equal to 4.2 mH when the command signal $\mathcal{S}$ is set to zero, but, when the command signal $\mathcal{S}$ is set to one, the equivalent value of L_{gr} reduces to 2.1 mH. In this test, the control gains are calculated considering only the nominal values of the LCL filter, meaning that the value of L_{gr} is not considered in the controller design. In addition, the information e_g about the grid voltage is assumed to be unknown for the controller; only the voltage measured at the point of common coupling PCC is fed to the controller. As before, the command active power P_{ref} is set to 1600 W, while the command reactive power Q_{ref} is set to be zero. This test was conducted considering a change in $\mathcal{S}$ as $\mathcal{S}: 0 \rightarrow 1$, which allows emulating a step decrease in the grid impedance as $L_{gr}: 4.2 \rightarrow 2.1$ mH. The experimental results of this test are presented in Fig. 13. The observed responses show that the proposed controller is able to maintain the stability of the closed-loop system for both values of L_{gr}. However, the results also show that the value of L_{gr} adversely impacts the quality of the grid current by increasing its level of harmonic distortion. More precisely, the total harmonic distortion (THD) of the grid current is found to be 3.9% when L_{gr} is set to 4.2 mH, but, when L_{gr} is reduced to 2.1 mH, the THD of the grid current is decreased to 3.5 %. Note that the THD of the grid current is found to be 1.7% when the grid inductance L_{gr} is neglected. The results obtained for different values of L_{gr} permits to conclude that the harmonic contents of the grid current increase as the grid inductance increases. What is worse, is that the closed-loop system can go unstable if the grid inductance is relatively very large. However, since a typical value of grid inductance is normally limited to some millihenries in low voltage distribution systems [44], it can be concluded that the proposed controller is able to maintain an acceptable current quality and a stable operation under a weak grid.

B. Performance Evaluation Under Unbalanced Grid Voltages

This test aimed to demonstrate the ability of the developed controller to cope with unbalanced grid voltages. Unbalance in grid voltages was created by changing the voltage magnitude of both phases "A" and "B", while the voltage magnitude of phase "C" remains unchanged. More precisely, the voltage magnitude was changed as $V_{LN_A} = 0.8V_{LN}$, $V_{LN_B} = 0.7V_{LN}$,

and $V_{LN_C} = V_{LN}$, with V_{LN} is the rms value of the grid voltage under normal conditions. In this test, the command active power was step changed as $P_{ref} : 0 \rightarrow 800 \rightarrow 1600$ W, while the command reactive power Q_{ref} was kept null. The current references $i_{g\alpha ref}$ and $i_{g\beta ref}$ are calculated based on the power command values and the measured grid voltages with the objective of delivering constant active power to the grid. Such an objective requires the three-phase currents to be sinusoidal, but with the amplitudes unbalanced to compensate for the unbalance in grid voltages. It is worth mentioning that the generation of the current references requires the use of the symmetrical components of the measured grid voltages. In this work, these voltage components are estimated using the phase-locked loop algorithm as presented in [43]. Fig. 14(a)–(d) shows reference and actual $\alpha - \beta$-axis components of grid currents, capacitor voltage of phase "A," active power P, reactive power Q, grid currents and converter-side currents,. Similar to the case of balanced grid voltages, the proposed controller was able to achieve fast and accurate control of the grid current even in the presence of voltage unbalance. The obtained results are almost the same as those obtained under balanced grid voltages except that the three-phase sinusoidal currents are with different amplitudes to maintain the active power P following a constant reference. It can also be observed that the reactive power Q oscillates with frequency $2\omega_f$, which is unavoidable to deliver constant active power to the grid under unbalanced grid voltages.

VII. Conclusion

This article has presented a robust active damping current controller for *LCL* filtered grid-connected VSI. The proposed current controller was constructed through combining a liner state-feedback control with a DOB. The state-feedback controller serves as a stabilizing controller while the disturbance observer plays the role of a servo-compensator to cancel the effect of parametric uncertainties on the control performances. The robust stability of the proposed controller was investigated in details through analyzing the closed-loop eigenvalues/poles of the uncertain state models. It was found that the proposed controller is able to ensure closed-loop stability under a wide range of model uncertainty. The proposed controller has been tested for performance evaluation using both simulation and experimentation. First, the obtained results have shown consistency between simulation and experimental results. Moreover, the experimental results have shown good abilities of the proposed controller to inject high-quality current into the grid with a fast, stable, robust, and accurate control. Finally, the obtained responses of the proposed controller are found to be robust to control saturation and changes in grid impedance.

Appendix
Design of the Resonant Controller

The resonant controller together with the capacitor current feedback is implemented as in [9] and [45]

$$u_\alpha = -K_c i_{c\alpha} + \left(K_p + \frac{2K_i\omega_c s}{s^2 + s2\omega_c + \omega_f^2}\right)(i_{g\alpha ref} - i_{g\alpha})$$

$$u_\beta = -K_c i_{c\beta} + \left(K_p + \frac{2K_i\omega_c s}{s^2 + s2\omega_c + \omega_f^2}\right)(i_{g\beta ref} - i_{g\beta}). \quad (93)$$

Following [9], it was found that $K_p = 35$, $K_i = 1000$, and

$$K_c = 2 \times 0.707 \times \sqrt{\frac{(L_c + L_g)\,L_c}{L_g C_f}}. \quad (94)$$

For purposes of digital implementation, the "Tustin with prewarping" approach is adopted to discretize the resonant term in the PR controller as presented in [45].

References

[1] W. Wu, Y. Liu, Y. He, H. S.-H. Chung, M. Liserre, and F. Blaabjerg, "Damping methods for resonances caused by LCL-filter-based current-controlled grid-tied power inverters: An overview," *IEEE Trans. Ind. Electron.*, vol. 64, no. 9, pp. 7402–7413, Sep. 2017.

[2] R. N. Beres, X. Wang, F. Blaabjerg, M. Liserre, and C. L. Bak, "Optimal design of high-order passive-damped filters for grid-connected applications," *IEEE Trans. Power Electron.*, vol. 31, no. 3, pp. 2083–2098, Mar. 2015.

[3] X. Wang, F. Blaabjerg, and P. C. Loh, "Grid-current-feedback active damping for LCL resonance in grid-connected voltage-source converters," *IEEE Trans. Power Electron.*, vol. 31, no. 1, pp. 213–223, Jan. 2016.

[4] W. Yao, Y. Yang, X. Zhang, F. Blaabjerg, and P. C. Loh, "Design and analysis of robust active damping for LCL filters using digital notch filters," *IEEE Trans. Power Electron.*, vol. 32, no. 3, pp. 2360–2375, Mar. 2017.

[5] R. Pena-Alzola, M. Liserre, F. Blaabjerg, M. Ordonez, and Y. Yang, "LCL-filter design for robust active damping in grid-connected converters," *IEEE Trans. Ind. Inform.*, vol. 10, no. 4, pp. 2192–2203, Nov. 2014.

[6] R. Errouissi, A. Al-Durra, and S. Muyeen, "Design and implementation of a nonlinear PI predictive controller for a grid-tied photovoltaic inverter," *IEEE Trans. Ind. Electron.*, vol. 64, no. 2, pp. 1241–1250, Feb. 2017.

[7] R. A. Fantino, C. A. Busada, and J. A. Solsona, "Optimum PR control applied to LCL filters with low resonance frequency," *IEEE Trans. Power Electron.*, vol. 33, no. 1, pp. 793–801, Jan. 2018.

[8] D. Pérez-Estévez, J. Doval-Gandoy, A. G. Yepes, Ó. López, and F. Baneira, "Enhanced resonant current controller for grid-connected converters with LCL filter," *IEEE Trans. Power Electron.*, vol. 33, no. 5, pp. 3765–3778, May 2018.

[9] Y. Jia, J. Zhao, and X. Fu, "Direct grid current control of LCL-filtered grid-connected inverter mitigating grid voltage disturbance," *IEEE Trans. Power Electron.*, vol. 29, no. 3, pp. 1532–1541, Mar. 2014.

[10] T. Hornik and Q.-C. Zhong, "A current-control strategy for voltage-source inverters in microgrids based on H_∞ and repetitive control," *IEEE Trans. Power Electron.*, vol. 26, no. 3, pp. 943–952, Mar. 2011.

[11] X. Hao, X. Yang, T. Liu, L. Huang, and W. Chen, "A sliding-mode controller with multiresonant sliding surface for single-phase grid-connected VSI with an LCL filter," *IEEE Trans. Power Electron.*, vol. 28, no. 5, pp. 2259–2268, May 2013.

[12] R. P. Vieira, L. T. Martins, J. R. Massing, and M. Stefanello, "Sliding mode controller in a multiloop framework for a grid-connected VSI with LCL filter," *IEEE Trans. Ind. Electron.*, vol. 65, no. 6, pp. 4714–4723, Jun. 2018.

[13] S. Kwak and S.-K. Mun, "Model predictive control methods to reduce common-mode voltage for three-phase voltage source inverters," *IEEE Trans. Power Electron.*, vol. 30, no. 9, pp. 5019–5035, Sep. 2015.

[14] N. Panten, N. Hoffmann, and F. W. Fuchs, "Finite control set model predictive current control for grid-connected voltage-source converters with LCL filters: A study based on different state feedbacks," *IEEE Trans. Power Electron.*, vol. 31, no. 7, pp. 5189–5200, Jul. 2016.

[15] J. C. Moreno, J. M. E. Huerta, R. G. Gil, and S. A. Gonzalez, "A robust predictive current control for three-phase grid-connected inverters," *IEEE Trans. Ind. Electron.*, vol. 56, no. 6, pp. 1993–2004, Jun. 2009.

[16] J. M. Espí, J. Castello, R. García-Gil, G. Garcera, and E. Figueres, "An adaptive robust predictive current control for three-phase grid-connected inverters," *IEEE Trans. Ind. Electron.*, vol. 58, no. 8, pp. 3537–3546, Aug. 2011.

[17] I. Sefa, S. Ozdemir, H. Komurcugil, and N. Altin, "An enhanced Lyapunov-function based control scheme for three-phase grid-tied VSI with LCL filter," *IEEE Trans. Sustain. Energy*, vol. 10, no. 2, pp. 504–513, Apr. 2019.

[18] N. Altin, S. Ozdemir, H. Komurcugil, and I. Sefa, "Sliding-mode control in natural frame with reduced number of sensors for three-phase grid-tied LCL-interfaced inverters," *IEEE Trans. Ind. Electron.*, vol. 66, no. 4, pp. 2903–2913, Apr. 2019.
[19] H. Li, W. Wu, M. Huang, H. S.-H. Chung, M. Liserre, and F. Blaabjerg, "Design of PWM–SMC controller using linearized model for grid-connected inverter with LCL filter," *IEEE Trans. Power Electron.*, vol. 35, no. 12, pp. 12773–12786, Dec. 2020.
[20] J. Fang, X. Li, X. Yang, and Y. Tang, "An integrated trap–LCL filter with reduced current harmonics for grid-connected converters under weak grid conditions," *IEEE Trans. Power Electron.*, vol. 32, no. 11, pp. 8446–8457, Nov. 2017.
[21] L. Huang, H. Xin, and F. Dörfler, "H_∞-control of grid-connected converters: Design, objectives and decentralized stability certificates," *IEEE Trans. Smart Grid*, vol. 11, no. 5, pp. 3805–3816, Sep. 2020.
[22] G. G. Koch, L. A. Maccari, R. C. Oliveira, and V. F. Montagner, "Robust $\mathcal{H}_\infty$ state feedback controllers based on linear matrix inequalities applied to grid-connected converters," *IEEE Trans. Ind. Electron.*, vol. 66, no. 8, pp. 6021–6031, Aug. 2019.
[23] C. R. D. Osório, G. G. Koch, H. Pinheiro, R. C. Oliveira, and V. F. Montagner, "Robust current control of grid-tied inverters affected by LCL filter soft-saturation," *IEEE Trans. Ind. Electron.*, vol. 67, no. 8, pp. 6550–6561, Aug. 2020.
[24] T. V. Tran, K.-H. Kim, and J.-S. Lai, "H_2/H_∞ robust observed-state feedback control based on slack LMI–LQR for LCL-filtered inverters," *IEEE Trans. Ind. Electron.*, vol. 70, no. 5, pp. 4785–4798, May 2023.
[25] W.-H. Chen, J. Yang, L. Guo, and S. Li, "Disturbance-observer-based control and related methods–An overview," *IEEE Trans. Ind. Electron.*, vol. 63, no. 2, pp. 1083–1095, Feb. 2016.
[26] N. B. Lai, K.-H. Kim, and P. Rodriguez, "Voltage sensorless control scheme based on extended-state estimator for a grid-connected inverter," *IEEE Trans. Power Electron.*, vol. 35, no. 6, pp. 5873–5882, Jun. 2020.
[27] W. Ma, Y. Guan, B. Zhang, and L. Wu, "Active disturbance rejection control based single current feedback resonance damping strategy for LCL-type grid-connected inverter," *IEEE Trans. Energy Convers.*, vol. 36, no. 1, pp. 48–62, Mar. 2021.
[28] D. Pérez-Estévez, J. Doval-Gandoy, A. G. Yepes, and Ó. López, "Positive- and negative-sequence current controller with direct discrete-time pole placement for grid-tied converters with LCL filter," *IEEE Trans. Power Electron.*, vol. 32, no. 9, pp. 7207–7221, Sep. 2017.
[29] H. Liao, X. Zhang, and Z. Ma, "Robust dichotomy solution-based model predictive control for the grid-connected inverters with disturbance observer," *CES Trans. Elect. Mach. Syst.*, vol. 5, no. 2, pp. 81–89, 2021.
[30] Y. Cai, Y. He, H. Zhou, and J. Liu, "Active-damping disturbance-rejection control strategy of LCL grid-connected inverter based on inverter-side-current feedback," *IEEE J. Emerg. Sel. Topics Power Electron.*, vol. 9, no. 6, pp. 7183–7198, Dec. 2021.
[31] G. Lou, W. Gu, J. Wang, J. Wang, and B. Gu, "A unified control scheme based on a disturbance observer for seamless transition operation of inverter-interfaced distributed generation," *IEEE Trans. Smart Grid*, vol. 9, no. 5, pp. 5444–5454, Sep. 2017.
[32] J. Liu, W. Wu, H. S.-H. Chung, and F. Blaabjerg, "Disturbance observer-based adaptive current control with self-learning ability to improve the grid-injected current for LCL-filtered grid-connected inverter," *IEEE Access*, vol. 7, pp. 105376–105390, 2019.
[33] Y. Wu and Y. Ye, "Internal model-based disturbance observer with application to CVCF PWM inverter," *IEEE Trans. Ind. Electron.*, vol. 65, no. 7, pp. 5743–5753, Jul. 2018.
[34] L. B. Freidovich and H. K. Khalil, "Performance recovery of feedback-linearization-based designs," *IEEE Trans. Autom. Control*, vol. 53, no. 10, pp. 2324–2334, Nov. 2008.
[35] K. J. Astrom and L. Rundqwist, "Integrator windup and how to avoid it," in *Proc. 1989 Amer. Control Conf.*, 1989, pp. 1693–1698.
[36] N. Bottrell and T. C. Green, "Comparison of current-limiting strategies during fault ride-through of inverters to prevent latch-up and wind-up," *IEEE Trans. Power Electron.*, vol. 29, no. 7, pp. 3786–3797, Jul. 2014.
[37] D. Pérez-Estévez, J. Doval-Gandoy, A. G. Yepes, Ó. López, and F. Baneira, "Generalized multifrequency current controller for grid-connected converters with LCL filter," *IEEE Trans. Ind. Appl.*, vol. 54, no. 5, pp. 4537–4553, Sep./Oct. 2018.
[38] H. K. Khalil, *Nonlinear Systems*, vol. 3. Upper Saddle River, NJ, USA: Prentice-Hall, 2002.
[39] J. Kukkola and M. Hinkkanen, "Observer-based state-space current control for a three-phase grid-connected converter equipped with an LCL filter," *IEEE Trans. Ind. Appl.*, vol. 50, no. 4, pp. 2700–2709, Jul./Aug. 2014.
[40] H. K. Khalil, *High-Gain Observers in Nonlinear Feedback Control*. Philadelphia, PA, USA: SIAM, 2017.
[41] E. Davison, "The output control of linear time-invariant multivariable systems with unmeasurable arbitrary disturbances," *IEEE Trans. Autom. Control*, vol. 17, no. 5, pp. 621–630, Oct. 1972.
[42] G. J. Balas, J. C. Doyle, K. Glover, A. Packard, and R. Smith, μ-*Analysis and Synthesis Toolbox*, vol. 72. Natick MA, USA: MUSYN Inc. and The MathWorks, 1993.
[43] P. Rodríguez, A. Luna, R. S. Muñoz-Aguilar, I. Etxeberria-Otadui, R. Teodorescu, and F. Blaabjerg, "A stationary reference frame grid synchronization system for three-phase grid-connected power converters under adverse grid conditions," *IEEE Trans. Power Electron.*, vol. 27, no. 1, pp. 99–112, Jan. 2012.
[44] A. Askarian, J. Park, and S. Salapaka, "Enhanced grid-following (E-GFL) inverter: A unified control framework for stiff and weak grids," *IEEE Trans. Power Electron.*, vol. 39, no. 5, pp. 5089–5107, May 2024.
[45] R. Teodorescu, F. Blaabjerg, M. Liserre, and P. C. Loh, "Proportional-resonant controllers and filters for grid-connected voltage-source converters," *IEE Proc. - Elect. Power Appl.*, vol. 153, no. 5, pp. 750–762, Sep. 2006.

Amulya Viswambharan received the B.Tech. degree in electrical and electronics engineering from Cochin University of Science and Technology, Kochi, India, in 2006, and the MTech. degree in power systems from the National Institute of Technology Calicut, Kozhikode, India, in 2014. She is currently working toward the Ph.D. degree in engineering from United Arab Emirates University, Al Ain, UAE.

Her research interests include nonlinear control, disturbance observer-based control, advanced control systems, artificial neural networks, and renewable energy conversion systems.

Rachid Errouissi (Senior Member, IEEE) received the Ph.D. degree in electrical engineering from the University of Quebec, Chicoutimi, QC, Canada, in 2010.

From 2011 to 2014, he was a Postdoctoral Researcher with the Department of ECE, University of New Brunswick, Fredericton, Canada. From 2014 to 2018, he was a Researcher/Teaching Associate with the Department of ECE, Khalifa University, PI campus, Abu Dhabi, UAE. He is currently an Associate Professor with the Department of ECE, United Arab Emirates University, Al Ain, UAE. His research interests include robust controls, disturbance observer approach, electric machines and drives, and renewable energy conversion systems.

Dr. Errouissi is a registered Professional Engineer in the province of New Brunswick, Canada.

Mahdi Debouza (Student Member, IEEE) received the B.Sc. degree from Abu Dhabi University, Abu Dhabi, UAE, in 2014, and the M.Sc. degree from Petroleum Institute, Khalifa University, Abu Dhabi, UAE, in 2016, both in electrical engineering. He is currently working toward the Ph.D. degree in electrical engineering with United Arab Emirates University, Al Ain, UAE.

From 2016 to 2021, he was a Research Assistant with Khalifa University, where he was involved in several research projects. His research interests include renewable energy control and integration, power quality, energy management and storage, microgrids, and smart grid technologies.

Hussain Shareef (Member, IEEE) received the Ph.D. degree in electrical engineering from Universiti Teknologi Malaysia (UTM), Johor Bahru, Malaysia, in 2007.

He is currently a Professor with the Department of Electrical Engineering, United Arab Emirates University (UAEU), Al Ain, UAE. He is also the Head of the Green Mobility Research Team with the Emirates Center for Mobility Research. He has authored or coauthored more than 400 peer-reviewed journal articles in various fields related to power and energy systems. He has more than 10 000 citations with an H-index of 52. His research interests include power system planning, integration of renewable power sources, application of AI techniques in power systems, energy management, power quality, and electric vehicle grid integration.

Dr. Shareef was a recipient of the UAEU Award for Excellence in Scholarship from 2019 to 2020 and the Chancellor Innovation Award from 2020 to 2021. He is a Member of the Mohammed Bin Rashid Academy of Scientists. He appeared as the World's Top 2% Scientist by Stanford University from 2019 to 2024.

Addy Wahyudie (Member, IEEE) received the B.Eng. degree in electrical engineering from Gadjah Mada University, Yogyakarta, Indonesia, in 2002, the M.Eng. degree in electrical engineering from Chulalongkorn University, Bangkok, Thailand, in 2005, and the D.Eng. degree in electrical engineering from Kyushu University, Fukuoka, Japan, in 2010.

From 2005 to 2011, he was a Lecturer with the Department of Electrical Engineering, Gadjah Mada University. In 2011, he joined as an Assistant Professor with United Arab Emirates University, Al Ain, UAE. He is currently an Associate Professor with the Department of Electrical Engineering, United Arab Emirates University. His research interests include control systems applications in electromechanical and renewable energy systems (ocean wave).